Localized dynamic patterns in the complex cubic-quintic Swift-Hohenberg equation in one and two dimensions

Hannes Uecker*
Institute for Mathematics, Carl von Ossietzky University of Oldenburg, Oldenburg, Germany

Nicolás Verschueren†
Physics Department, University of California at Berkeley, Berkeley CA 94720, USA
Department of Mathematics and Statistics, University of Exeter, Exeter, UK
EPSRC Hub for Quantitative Modelling in Healthcare,University of Exeter, Exeter, UK and
Living Systems Institute, University of Exeter, Exeter, UK

Edgar Knobloch‡
Physics Department, University of California at Berkeley, Berkeley CA 94720, USA
(Dated: February 25, 2026)

We use bifurcation analysis and numerical methods to study dynamic patterns in a complex Swift-Hohenberg equation in one (1D) and two (2D) dimensions, focusing on structures present on a 1D interval and a 2D disk. Periodic boundary conditions are imposed on the spatial variable in 1D and on the angular variable in 2D. In 1D the equation features Hopf bifurcations from the trivial state $u \equiv 0$ at finite wave number $k \neq 0$ (also known as wave bifurcations) leading to a bifurcation problem with $O(2) \times \mathcal{S}^1$ symmetry, i.e., symmetry under translations and reflections in space, and phase rotations. The $O(2)$ symmetry implies the simultaneous appearance of traveling waves and standing waves, and we consider the case where both bifurcations are subcritical and yield secondary bifurcations to spatially localized structures in the form of modulated traveling waves and localized standing waves, respectively. We use numerical continuation to show that some of the branches thus obtained exhibit homoclinic snaking associated with their gradual growth in spatial extent. We exploit the gauge symmetry to compute these dynamic patterns as relative equilibria, which allows to efficiently find tertiary bifurcations to 2-frequency localized standing waves, and to localized drifting waves. The intricate behavior identified in 1D is shown to provide a "road map" for the organization of wall-attached states on 2D disks in the form of rotating and standing waves at the wall, which may further localize in angle, yielding rotating spots or stationary breathing spots at the wall, and tertiary bifurcations from these. Some direct numerical simulations are used to identify further structures, including dynamics present in the disk bulk.

Dynamic patterns on finite disks arise in various contexts including combustion, nonlinear optics, and fluid dynamics, yielding a variety of rotating and breathing structures. Here we study bifurcation diagrams for such states in the complex Swift–Hohenberg equation when the zero solution loses stability with respect to subcritical rotating and standing waves. Such states may be supported in the disk bulk or confined to the disk boundary. In the latter case, secondary bifurcations lead to wall-attached rotating and standing waves that may also localize in angle. These wall states are shown to exhibit behavior similar to that of localized traveling and standing waves on a one-dimensional (1D) interval with periodic boundary conditions. As a result the 1D case provides a road map for the very rich zoo of wall states in 2D. We use bifurcation analysis together with numerical continuation to study the branching behavior and stability properties of these dynamic patterns, leveraging the invariance of the complex Swift–Hohenberg equation under phase rotations. The results are complemented by direct numerical simulations of the wall states and their interaction with the bulk.

I. INTRODUCTION

Pattern formation on finite disks arises naturally in various contexts including combustion [GHEHR94, PGGR97, BGP05], nonlinear optics [LPRT96, DKJ+00] and fluid dynamics [ZES93, BT06, BT10a, BT10b, FK20], resulting in a variety of rotating or breathing structures in both experiments and associated numerical studies of model equations. These structures may be spatially extended, a property usually associated with supercritical bifurcations, or spatially localized, as commonly found in systems with a subcritical primary instability. Existing studies have largely focused on the former case and the resulting rotating and ratcheting states which are amenable to both experimental study and direct numerical simulation [GHEHR94, PGGR97, BGP05]. In the latter case, which arises in some fluid systems, such a binary fluid convection in a cylinder [MAB08], our under-

* hannes.uecker@uni-oldenburg.de
† n.verschueren-van-rees@exeter.ac.uk
‡ knobloch@berkeley.edu

standing remains rather incomplete. This case is much richer, however, in that secondary instabilities from spatially periodic structures may lead to spatial localization and thus a much greater variety of time-dependent states. Recent work employing the real Swift-Hohenberg equation reveals the wealth of behavior that results from spatial localization on a disk even in the simplest case, that of a variational system exhibiting subcritical steady state primary bifurcation [VKU21].

Here we extend this work to the dynamic case resulting from of a subcritical symmetry-breaking Hopf bifurcation on a disk, i.e. a wave bifurcation. Owing to the symmetry of the problem under spatial rotations and reflections, the wave bifurcation results in two distinct spatially periodic states, rotating waves (RWs) and standing waves (SWs) (see Table I for a summary of acronyms used here). The former are relative equilibria, i.e., steady states in the corotating frame; the latter are time-periodic breathing states that preserve reflection symmetry at all times. Both states may bifurcate subcritically in which case they are susceptible to secondary bifurcations resulting in spatial localization. We refer to the states generated from spatial modulational instabilities of RWs as modulated RWs (MRWs). In contrast, a spatial modulational instability of SWs results in localized standing waves (LSWs); these come in two families, even and odd with respect to the symmetry axis of the underlying SW, implying that the oscillations on either side of the symmetry axis are in phase (even case) or out of phase (odd case).

As shown here, the LSWs may exhibit homoclinic snaking, well known from localized steady patterns [BK07]: the odd and even LSW lie on a pair of intertwined branches in parameter space, with each LSW adding half a wavelength on either side in passing from a fold to the next fold above it, until the avalaible domain is filled with a SW. Additionally, the LSW branches are cross-linked by branches of localized drifting waves (LDWs) created in *drift bifurcations* [KM95, GBM$^+$04], i.e., by branches of two-frequency states. The drift speed s of these states can have either sign, and vanishes at either end. In other parameter regimes, the LDW branches do not form such interconnecting rung states but instead develop $O(1)$ speeds away from onset and characteristics of MRWs.

All of these states come, in general, in two flavors: they can be supported in the disk bulk or take the form of wall states supported at the disk boundary. Mixed states are also possible. We focus here mostly on the wall states and leverage their similarity to like states on a periodic interval to generate a road map for the wall states identified in two spatial dimensions (2D). In particular, the (modulated) rotating waves (RWs) found in 2D correspond to (modulated) traveling waves in 1D. Figure 1 and Table II compare the 1D and 2D states and their symmetries.

The results reported here are based on a prototypical model system offering a good compromise between simplicity and dynamical richness. Specifically, we consider the *complex* cubic-quintic Swift-Hohenberg equation (CSHE35),

TABLE I. Acronyms.

Acronym	**Meaning**
AE	amplitude equation
BD	bifurcation diagram
BP, HP	branch point, Hopf point
DNS	direct numerical simulation
NBC	Neumann boundary condition
IC	initial condition
pBC	periodic boundary condition
PO	(time-)periodic orbit
RSHE35	real cubic–quintic Swift–Hohenberg equation
CSHE35	complex cubic–quintic Swift–Hohenberg equation

$$\begin{aligned}\partial_t u =&(\lambda+\mathrm{i}\nu)u-(c_3+\mathrm{i}\gamma)|u|^2u-|u|^4u \\ &-(1+\nabla^2)^2u+\mathrm{i}\delta\nabla^2u,\end{aligned} \tag{1}$$

with $u=u(x,t)\in\mathbb{C}$, and coefficients $\lambda,\nu,\delta,c_3,\gamma\in\mathbb{R}$, cf. [Mal84, SB98, SCA02, AA05, GK11]. The model (1) is a generalization of the well-known complex Ginzburg-Landau equation [AK02], and simultaneously a generalization of the real SH35 equation (RSHE35) studied in [VKU21]. The CSHE35 equation has been studied in both 1D and 2D using DNS [SB98, GK11], see also [LMN94, SCA02], albeit not on a disk, yielding many distinct localized structures at selected parameter values, but without attempting to construct the corresponding bifurcation diagrams (BDs) that would describe their origin and properties as parameters are varied. Such BDs are constructed here using numerical continuation of solutions in both 1D and 2D.

We study (1) on a 1D interval and a 2D disk, namely

$$\Omega_1=[-\ell/2,\ell/2), \tag{2a}$$
$$\Omega_2=\{\mathbf{x}{=}r(\cos\vartheta,\sin\vartheta):r{\in}[0,R],\vartheta{\in}[-\pi,\pi)\}. \tag{2b}$$

For the 1D problem we use periodic boundary conditions (pBCs), given in the phase space $H^4(\Omega_1)$ by

$$\partial_x^j u(-\ell/2)=\partial_x^j u(\ell/2),\quad j=0,\dots,3, \tag{3a}$$

for a domain of length ℓ, while in 2D we use Neumann boundary conditions (NBCs)

$$\nabla u\cdot\hat{n}|_{\partial\Omega_2}=0,\quad \nabla(\nabla^2u)\cdot\hat{n}|_{\partial\Omega_2}=0, \tag{3b}$$

where $\hat{n}$ represents the outward unit normal.

We begin with the 1D case, which besides being of interest in its own right also provides a "road map" for the organization of the wall-attached solutions on a disk, i.e., solutions that are a consequence of the presence of the disk boundary. We start with the "base parameter set" $c_3=-2.5$ and

$$(\nu,\gamma,\delta)=(-1,0.5,1), \tag{4}$$

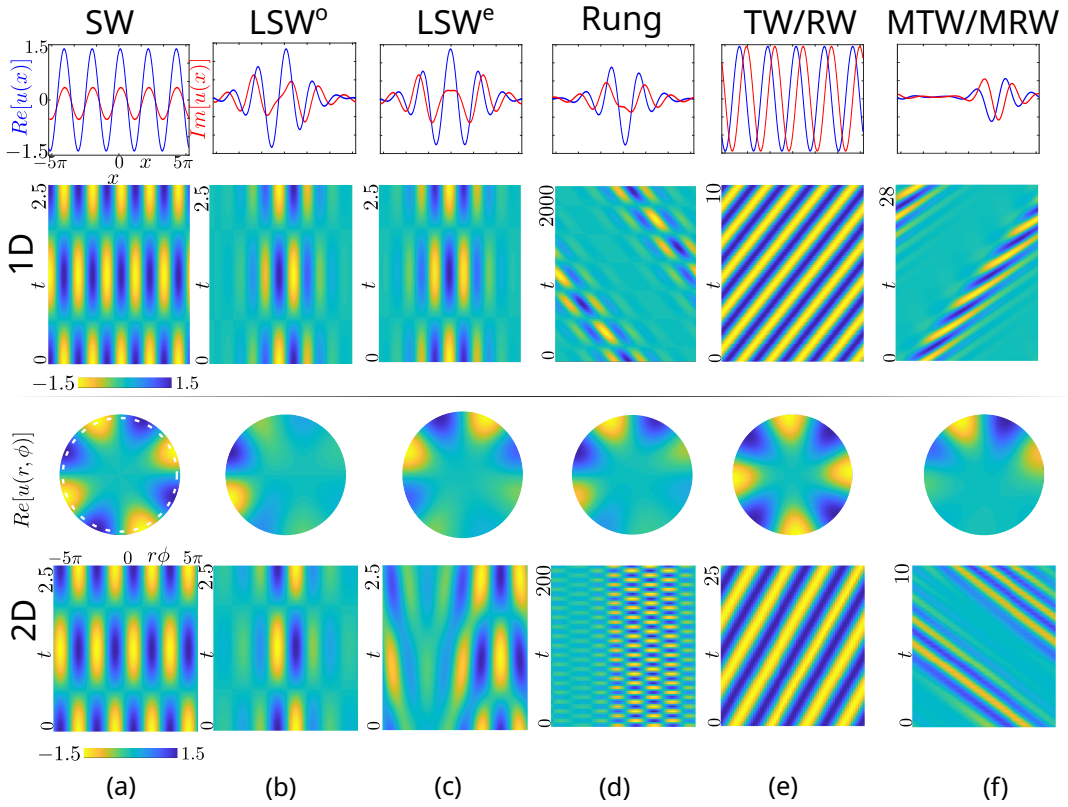

FIG. 1. Selection of states observed in (1), in 1D (top, $\Omega_1 = [-5\pi, 5\pi)$) and 2D (bottom, $\Omega_2 = \{(r,\phi) : r \in [0,5], \vartheta \in [0,2\pi)\}$), $(\nu, c_3, \gamma, \delta) = (-1, -2.5, 0.5, 1)$, and λ near -1, i.e., in the subcritical range. This regime supports (a) standing (SW) and (e) traveling (TW) resp. rotating (RW) waves, as well as localized versions, namely localized SWs with (b) an odd (LSW^o) and (c) even (LSW^e) spatial profile; (d) shows asymmetric (and traveling) rung states, and (f) shows modulated TWs (MTW). In the space–time plots for 2D at the bottom, space runs along the perimeter of the disk.

with λ as the primary bifurcation parameter. This choice is explained below.

Figure 1 illustrates the states arising from a finite wave number Hopf instability of the trivial state $u \equiv 0$, $\lambda \in \mathbb{R}$, in the presence of $O(2)$ symmetry in both 1D and 2D; similar states can be found in other $O(2)$-equivariant systems, including reaction-diffusion systems exhibiting a wave bifurcation [KUY21, KMUY26]. However, the computations here are greatly simplified by the additional $\mathcal{S}^1$ phase invariance of (1). Specifically, in 1D the $O(2)$ symmetry is generated by continuous translations $x \mapsto x+\xi$, $\xi \in [0, \ell)$ together with the reflection symmetry $x \mapsto -x$, while in 2D it is a consequence of rotations and reflections in the angle ϑ. The phase equivariance, which in the following we call *gauge invariance* to distinguish it from the phase conditions used below, implies that if $u(x,t)$ is a solution, so is $u(x,t)\mathrm{e}^{\mathrm{i}\theta}$ for any $\theta \in [0, 2\pi)$. As a result the full symmetry group is $O(2) \times \mathcal{S}^1$ in both cases.

In both cases, Ω_1 and Ω_2, the trivial solution $u \equiv 0$ of (1) is stable for $\lambda < \lambda_c$ and unstable for $\lambda > \lambda_c$, with $\lambda_c \approx 0$ depending on the (size of the) domain. We start with the computation of branches of TWs (1D) and RWs (2D), stemming from the trivial branch $u \equiv 0$ at the BPs $\lambda_j \geq \lambda_c$. The 1D TWs are given by the single mode expression

$$u_{\mathrm{TW}}(x,t) = \alpha \mathrm{e}^{\mathrm{i}(kx - \omega_{\mathrm{TW}} t)}, \tag{5}$$

with explicit expressions for the amplitude α and frequency ω_{TW}, namely

$$\alpha^2 = -\frac{c_3}{2} \pm \sqrt{\frac{c_3^2}{4} + \lambda - (1-k^2)^2}, \tag{6}$$

$$\omega_{\mathrm{TW}} = -\nu + \gamma\alpha^2 + \delta k^2. \tag{7}$$

In particular, $|u_{\mathrm{TW}}| = \alpha$ is a constant. An alternative way of writing u_{TW} is

$$u_{\mathrm{TW}}(x,t) = \alpha \mathrm{e}^{\mathrm{i}k(x-st)}, \quad s = \omega_{\mathrm{TW}}/k, \tag{8}$$

using the (phase) speed s of the TW instead of its frequency ω_{TW}.

The 2D RWs are slightly more complicated:

$$u_{\mathrm{RW}}(x,t) = \left(\sum_{l \in \mathbb{N}} J_m(k_{m,l} r) \right) \mathrm{e}^{\mathrm{i}(m\vartheta - \omega_{\mathrm{RW}} t)}, \tag{9}$$

where $x = r\mathrm{e}^{\mathrm{i}\vartheta}$ (in polar coordinates), J_m is the mth Bessel function of the first kind, and $k_{m,l} = \alpha_{m,l}/R$, with $\alpha_{m,l}$ the lth zero of J'_m. Note that u_{RW} still consists of

TABLE II. Solution classes and symmetries; in 2D (bottom half) we use (r,ϑ) for the polar coordinates on the disk.

Type	**order**	**origin, form and symmetries**
TW	prim.	traveling wave, bifurcating from $u\equiv 0$, $u_{\mathrm{TW}}(x,t)=\alpha \mathrm{e}^{\mathrm{i}(kx-\omega_{\mathrm{TW}}t)}$, see (5); $\lvert u\rvert$ constant in space and time, relative equilibrium in comoving frame with speed $s=\omega_{\mathrm{TW}}/k$.
SW	prim.	standing wave, bifurcating from $u\equiv 0$, $u_{\mathrm{SW}}(x,t)=v(x)\mathrm{e}^{-\mathrm{i}\omega_{\mathrm{SW}}t}$, see (34); $\lvert u\rvert$ constant in time, relative equilibrium in gauge rotating frame.
MTW	second.	modulated TW, bifurcating from TWs, $u_{\mathrm{MTW}}(x,t)=v(x-s_2t)\mathrm{e}^{\mathrm{i}(kx-\omega t)}$, see (37), but (numerically) computed as relative PO in frame with (average) speed s; $\lvert u\rvert$ constant in time in frame moving with speed s_2, with $s_2=\mathcal{O}(1)$ in general, in particular at onset.
LSW	second.	localized standing wave, bifurcating from SWs, same form as SW, with spatially localized v.
LDW	tert.	localized drifting wave, $u_{\mathrm{LDW}}(x,t)=v(x-st)\mathrm{e}^{-\mathrm{i}\omega t}$, bifurcating from LSWs in a drift bifurcation, i.e., with speed $s=0$ at onset; relative equilibrium in comoving and gauge rotating frame.
2-freq.LSW	tert.	two-frequency LSW, bifurcating from LSWs, $u(x,t)=v(x,t)\mathrm{e}^{-\mathrm{i}\omega t}$ with v periodic in time with period $T>0$, $\lvert u\rvert$ not constant in space or time. Similarly for 2-freq. SWs, which bifurcate from SWs.
RW	prim.	rotating wave, bifurcating from $u\equiv 0$, $u_{\mathrm{RW}}(x,t)=v(r)\mathrm{e}^{\mathrm{i}(m\vartheta-\omega_{\mathrm{RW}}t)}$, see (9); $\lvert u\rvert$ constant in ϑ,t, relative equilibrium in corotating frame with speed $s=\omega_{\mathrm{RW}}/m$.
SW	prim.	standing wave, bifurcating from $u\equiv 0$, like 1D (dimension-indep.), $u_{\mathrm{SW}}(x,t)=v(x)\mathrm{e}^{-\mathrm{i}\omega_{\mathrm{SW}}t}$, see (34).
MRW	second.	modulated RW, bifurcating from RWs, $u_{\mathrm{MRW}}(x,t)=v(r,\vartheta-s_2t))\mathrm{e}^{\mathrm{i}(m\vartheta-\omega_{\mathrm{RW}}t)}$, but (numerically) computed as relative PO in frame rotating with (average) speed s; $\lvert u\rvert$ constant in time in frame rotating with speed s_2.
LSW	second.	localized SW, bifurcating from SWs, with $v(x)$ localized in angle ϑ.
LDW	tert.	as in 1D, bifurcating from LSWs, with drift in ϑ.
2-freq.LSW	tert.	two-frequency LSW, as in 1D, bifurcating from LSWs.

a single mode in ϑ and that $|u_{\mathrm{RW}}|$ is therefore constant in ϑ.

As already mentioned, the $O(2)$ symmetry of (1) implies additional sets of primary solution branches, namely standing waves (SWs) u_{SW}. These bifurcate together with the TWs (RWs) from the respective BPs and resemble equal amplitude superpositions of left and right TWs (RWs) near onset [Kno86]. By the gauge invariance of (1), $|u_{\mathrm{SW}}|$ is again constant in time, in both 1D and 2D, i.e., the SWs take the form $u(x,t)=v(x)\mathrm{e}^{-\mathrm{i}\omega_{\mathrm{SW}}t}$ (and hence could be called rotating gauge waves) but v is no longer a single mode but contains all odd harmonics of $\mathrm{e}^{\mathrm{i}k_jx}$, viz. $\mathrm{e}^{\mathrm{i}mk_jx}, m=2n+1, n\in\mathbb{Z}$ (1D), resp. higher Bessel modes (2D). Thus, there is no explicit formula for SWs at finite amplitude although, as shown below, they can be approximated very accurately by amplitude equations employing only a few modes even far from onset.

Beyond the bifurcations of the primary TW/RW and SW branches from $u\equiv 0$, we are interested in secondary bifurcations, and these are particularly rich if the primary bifurcations are subcritical, i.e., towards $\lambda<\lambda_c$. The secondary bifurcations of main interest are those to localized SWs (LSWs) from the SWs, and to modulated TWs (MTWs) from the TWs, see Figs. 1(b-d) and (f) for illustration. The branches and bifurcations depend on the parameters heuristically as follows: ν and δ set the initial frequency ω, while γ determines how ω changes with $|u|^2=\alpha^2$ along the TW branch, see (7), and similarly for SW. Qualitatively similar behavior is present in 2D as well.

Together these observations motivate our choice of parameters focusing on the subcritical case $c_3=-2.5<0$. While ν can be scaled out by going into a rotating frame $u\mapsto \mathrm{e}^{\mathrm{i}\nu t}u$, it turns out that it is more convenient to start with $\nu=-1$, and combine this with $\delta=1$ to generate finite speeds $s=\pm 2$ (1D) at onset. This speed increases with $|u|$ when $\gamma>0$ but decreases with $|u|$ when $\gamma<0$, and therefore besides (4) we also use the parameter sets (keeping $c_3=-2.5$ throughout)

$$(\nu,\gamma,\delta)=(0,-0.5,1), \tag{10}$$
$$(\nu,\gamma,\delta)=(0,-1,0.5), \tag{11}$$

again with λ as the primary bifurcation parameter. Here smaller values of δ favor SWs over TWS (in the sense of dynamical stability) and their secondary bifurcations to LSW and while larger δ favors TWs and their secondary bifurcations to MTWs. Beyond the secondary bifurcations to MTWs/MRWs and LSWs, we also identify tertiary bifurcations from LSWs, namely to *localized drifting waves* (LDWs) and to *two-frequency* LSWs, see Table II, and the discussion before (1).

The rest of the paper is organized as follows. Sections II and III describe our 1D and 2D results. In both sections, we start with analytical approximations to the primary solution branches (TWs/RWs and SWs) followed by numerical results confirming the analysis, and then turn to secondary and tertiary bifurcations. We start with the base parameter set (4), and subsequently explain the impact of changing to the parameter sets (10) and (11). In 2D we demonstrate that the wall-attached states exhibit behavior analogous to that in 1D with localization in angle playing the role of localization in x, as illustrated in Fig. 1. We also comment briefly on bulk

mode branches, and present DNS results initialized from different unstable states. The numerical continuation results and the bifurcations from both (relative) equilibria and genuine time periodic orbits (POs) are computed using the package `pde2path` [Uec21, pde25]; this package is also used for the DNS. Some details of the numerical method, e.g., how to take advantage of the system symmetries, are included in §II B. In §IV we summarize our results and relate them to existing work on more complex systems with $O(2)$ symmetry and wave bifurcations.

II. 1D CASE: FINITE DOMAIN WITH PERIODIC BOUNDARY CONDITIONS

The starting point of the bifurcation analysis is the linearization of (1) at the trivial solution branch $u \equiv 0$, $\lambda \in \mathbb{R}$, i.e., $\partial_t v = \mathcal{L}v \equiv [\lambda + \mathrm{i}\nu - (1+\Delta)^2 + \mathrm{i}\delta\Delta]v$. Over Ω_1, the ansatz $v = \alpha \mathrm{e}^{\mathrm{i}kx+\mu(k)t}$ with $k = k_j \equiv 2\pi j/\ell$ yields the dispersion relation

$$\mu(k) = \lambda + \mathrm{i}\nu - (1-k^2)^2 - \mathrm{i}\delta k^2. \tag{12}$$

In particular, the branch points (BPs) $\lambda = \lambda_j \equiv (1-k_j^2)^2$ lead to the TW branches u_{TW} with wave numbers k_j and speeds $s_j \equiv \mp|\omega_j|/k_j$ for left- and right-traveling waves, respectively. Here $\omega_j = -\nu + \delta k_j^2$, and due to the gauge invariance of (1) these are in fact single mode solutions with the explicit expression (5). The $O(2)$ symmetry of (1) further implies the presence of standing waves $u(x,t) = v(x)\mathrm{e}^{-\mathrm{i}\omega_{\mathrm{SW}}t}$ but v is no longer a single mode but contains all odd harmonics of $\mathrm{e}^{\mathrm{i}k_j x}$, i.e., $\mathrm{e}^{\mathrm{i}mk_j x}, m = 2n+1, n \in \mathbb{Z}$. Before proceeding to the numerical computation of these branches and their secondary bifurcations, we derive the associated amplitude equations (AEs), which are shown to yield an excellent agreement with the continuation results for the primary branches.

A. 1D amplitude equations

We are particularly interested in AEs describing subcritical TWs and SWs *far from onset*, a regime inaccessible using a formal asymptotic expansion in a small parameter. These primary branches bifurcate together from $u \equiv 0$ with wave numbers $k = k_j \in \mathbb{R}$ and can be approximated by a modal expansion as done, for example, in [DKW81], see also [BMvS09, Method II], implicitly treating the higher modes as fully slaved to the leading ones. More precisely, we make the ansatz (see Remark II.1 for an extension to higher order modes)

$$u(x,t) = [v(t)e^{ikx} + w(t)e^{-ikx}]e^{-i\omega t} \tag{13}$$

with no *a* priori assumption on the magnitude of the amplitudes v and w. With the notation $e_j \equiv \exp \mathrm{i}jkx$ we see that $\mathcal{L} \equiv \lambda + \mathrm{i}\nu - (1+\Delta)^2 + \mathrm{i}\delta\Delta$ acts on ve_k as

$$\mathcal{L}(ve_k) = \mu(k)e_k, \quad \mu(k) = \lambda + \mathrm{i}\nu - (1-k^2)^2 - \mathrm{i}\delta k^2 \tag{14}$$

and moreover that

$$|u|^2 = v\overline{w}e_2 + \alpha + w\overline{v}e_{-2}, \tag{15}$$

$$|u|^2 u = \big(v^2\overline{w}e_3 + \beta_1 ve_1 + \beta_2 we_{-1} + w^2\overline{v}e_{-3}\big)\mathrm{e}^{-\mathrm{i}\omega t}, \tag{16}$$

$$\begin{aligned} |u|^4 u = \Big(& v^3\overline{w}^2 e_5 + (\beta_1 v^2\overline{w} + \alpha v^2\overline{w})e_3 \\ & + (\beta_2|w|^2 + \alpha\beta_1 + |v|^2|w|^2)ve_1 \\ & + (\beta_1|v|^2 + \alpha\beta_2 + |v|^2|w|^2)we_{-1} \\ & + (\alpha w^2\overline{v} + \beta_2 w^2\overline{v})e_{-3} + w^3\overline{v}^2 e_{-5}\Big)\mathrm{e}^{-\mathrm{i}\omega t}, \end{aligned} \tag{17}$$

where $\alpha \equiv |v|^2 + |w|^2$, $\beta_1 \equiv \alpha + |w|^2$, $\beta_2 \equiv \alpha + |v|^2$.

In the following we focus on the primary branches bifurcating from $u \equiv 0$ at the first BP (when $\ell = 10\pi$ as in Fig. 1, this occurs at $\lambda_c = 0$ with $k_c = 1$) and hence set $k = 1$. Substituting (13) into (1) and collecting terms of the form $e_1\mathrm{e}^{-\mathrm{i}\omega t}$ and $e_{-1}\mathrm{e}^{-\mathrm{i}\omega t}$ yields the AEs

$$\dot v = \mathrm{i}(\nu + \omega - \delta - \gamma\beta_1)v + (\lambda - c_3\beta_1 - c_{51})v, \tag{18a}$$

$$\dot w = \mathrm{i}(\nu + \omega - \delta - \gamma\beta_2)w + (\lambda - c_3\beta_2 - c_{52})w, \tag{18b}$$

where $c_{51} \equiv 2\alpha|w|^2 + \alpha^2 + 2|v|^2|w|^2$, $c_{52} \equiv 2\alpha|v|^2 + \alpha^2 + 2|v|^2|w|^2$. Thus, writing $v = r_1\mathrm{e}^{\mathrm{i}\phi_1}$ and $w = r_2\mathrm{e}^{\mathrm{i}\phi_2}$, we obtain

$$\dot r_1 = [\lambda - c_3\beta_1 - c_{51}]r_1, \quad \dot r_2 = [\lambda - c_3\beta_2 - c_{52}]r_2, \tag{19a}$$

$$\dot\phi_1 = \nu + \omega - \delta - \gamma\beta_1, \quad \dot\phi_2 = \nu + \omega - \delta - \gamma\beta_2. \tag{19b}$$

We are interested in steady states of (19) in the form of TWs ($r_1 r_2 = 0$) and SWs ($r_1 = r_2 \neq 0$). For TWs with $r_1 > 0$ and $r_2 = 0$ we obtain $\alpha = r_1^2$, $\beta_1 = r_1^2$, $c_{51} = r_1^4$, resulting in the fixed point

$$\begin{aligned} r_{\mathrm{TW}}^2 &= -\frac{c_3}{2} \pm \sqrt{\frac{c_3^2}{4} + \lambda}, \\ \omega_{\mathrm{TW}} &= -\nu + \delta + \gamma r_{\mathrm{TW}}^2 \end{aligned} \tag{20}$$

as obtained already in (7), and yielding a TW fold at

$$\lambda = \lambda_f = -c_3^2/4, \qquad c_3 < 0. \tag{21}$$

For SWs with $r_1 = r_2 =: r \neq 0$ we obtain $\alpha = 2r^2$, $\beta_1 = \beta_2 = 3r^2$, $c_{51} = c_{52} = 10r^4$ yielding the fixed point

$$\begin{aligned} r_{\mathrm{SW}}^2 &= -\frac{3c_3}{20} \pm \sqrt{\frac{9c_3^2}{400} + \frac{\lambda}{10}}, \\ \omega_{\mathrm{SW}} &= -\nu + \delta + 3\gamma r_{\mathrm{SW}}^2, \end{aligned} \tag{22}$$

with a SW fold at

$$\lambda = \lambda_f = -\frac{9}{40}c_3^2, \qquad c_3 < 0. \tag{23}$$

It turns out that these approximate expressions provide an excellent fit with the numerics for the SWs that bifurcate from $u = 0$ at $\lambda = 0$, cf. Fig. 2. Moreover, if, e.g., $\delta > 0$ and $\gamma < 0$, then $\omega_{\mathrm{SW}} = 0$ at

$$\lambda_c = 10\left[\left(\frac{3c_3}{20} + \frac{\nu - \delta}{3\gamma}\right)^2 - \frac{9c_3^2}{400}\right], \tag{24}$$

a result that will be used in Section II D below.

Remark II.1. The natural form for a higher order ansatz is

$$u(x,t) = \Big[v(t)e^{ikx} + w(t)e^{-ikx} + v_3(t)e^{3ikx} + w_3(t)e^{-3ikx}\Big]e^{-i\omega t}. \quad (25)$$

Then treating v_3 and w_3 adiabatically, i.e., assuming that $v_3 = w_3 = \mathcal{O}(\varepsilon^3)$ and $\dot v_3 = \dot w_3 = \mathcal{O}(\varepsilon^5)$ in a formal ε expansion, we obtain

$$\begin{aligned} e_3:\ & 0 = \mu(3)v_3 - (c_3+\mathrm{i}\gamma)v^2\overline{w} - v^2\overline{w}(\beta_1+\alpha) \\ \Leftrightarrow\ & v_3 = \frac{1}{\mu(3)}\big[(c_3+\mathrm{i}\gamma)v^2\overline{w} + (2|w|^2+|v|^2)\overline{w}v^2\big], \quad (26)\\ e_{-3}:\ & w_3 = \frac{1}{\mu(-3)}\big[(c_3+\mathrm{i}\gamma)w^2\overline{v} + (2|v|^2+|w|^2)\overline{v}w^2\big]. \end{aligned} \quad (27)$$

To leading order, v_3 and w_3 must then be included in $-(c_3+\mathrm{i}\gamma)|u|^2u = -(c_3+\mathrm{i}\gamma)\big[(16) + (v_3\overline{v}+\overline{w}_3w)we_1 + (w_3\overline{w}+\overline{v_3}v)ve_{-1}\big]$, which yields corrections to c_{51} and c_{52} in (18). For TWs we still have $v_3 = w_3 \equiv 0$ as only products of v and w appear in (26) and (27), and of course this agrees with the single mode exact expression (7). For SWs, the higher modes $v_3e_3 + w_3e_{-3} \neq 0$ (in fact $v_je_j \neq 0$, $w_je_{-j} \neq 0$ for all $j = 2k+1$, $k \in \mathbb{N}$), and (26) and (27) should in principle be taken into account. However, because

$$|\mu(\pm 3)| = |\lambda - 64 + \mathrm{i}(\nu+\omega-9\delta)| \quad (28)$$

is rather large (a benefit of the rather strong linear damping in the CSHE away from the critical modes, and the cubic-quintic nonlinearity which only generates odd modes), the higher order modes v_3 and w_3 are quite small in the parameter regimes considered below, and so may be safely neglected. See, e.g., the FFT plot of SW in Fig. 2. ⌋

Remark II.2. For suitable choice of parameters, e.g., $\gamma < 0$ and $\delta > 0$, (7) shows that TWs can have zero speed, i.e., for $\omega_{\mathrm{TW}} \equiv -\nu + \gamma\alpha^2 + \delta k^2 = 0$ we have an exact steady state $u^{(0)}_{\mathrm{TW}} = \alpha \mathrm{e}^{\mathrm{i}kx}$ at an isolated value of λ. Similarly, the temporal frequency ω_{SW} of SWs can also go to zero (period $T \to \infty$, see (22) for an approximate expression for ω_{SW}), resulting in an (approximate) spatially periodic steady state $u^{(0)}_{\mathrm{SW}}$ at an isolated λ value, which we then compute numerically, with excellent agreement. The $u^{(0)}_{\mathrm{SW}}$ are different from $u^{(0)}_{\mathrm{TW}}$, in particular $|u^{(0)}_{\mathrm{SW}}|$ is not spatially constant. ⌋

B. Numerical continuation and bifurcation

For an exposition of numerical continuation for PDEs, including the software `pde2path` used here and downloadable at [pde25], we refer to [Uec21]. In our 1D numerics, (1) is always solved in a frame moving with speed $s(t) = \dot\sigma(t)$ (possibly $s = 0$), i.e., we set $\tilde u(x,t) = u(x-\sigma(t),t)$ and after dropping the tilde we obtain

$$\begin{aligned} \partial_t u =& (\lambda+\mathrm{i}\nu)u - (c_3+\mathrm{i}\gamma)|u|^2u - |u|^4u \\ & - (1+\partial_x^2)^2u + \mathrm{i}\delta\partial_x^2u + s\partial_x u. \end{aligned} \quad (29)$$

In particular, TWs are equilibria of (29) with constant s (relative equilibria), where $s > 0$ corresponds to right-traveling waves, while $s < 0$ corresponds to left-traveling waves. To compute TWs numerically we set the time derivatives to zero in (29) and solve the resulting nonlinear eigenvalue problem for (u,s) using the phase condition

$$q(u) := \langle \partial_x u_{\mathrm{old}}, u\rangle = 0, \quad (30)$$

where u_{old} is the solution from the last continuation step, and $\langle f,g\rangle := \int_\Omega f(x)g(x)\,\mathrm{d}x$. This removes the translational zero eigenvalue with eigenfunction $\partial_x u$ from the linearization of (29) around a nontrivial $u(x)$, and makes the continuation orthogonal to the group orbit of translations $T_\xi u = u(x-\xi)$.

Because of the explicit formula (7), a numerical computation of TWs is not in fact necessary, but is used here as a starting point for MTWs. For the sake of generality (see Remark II.3), these are computed as time–periodic orbits (POs) in a comoving frame. For this we have two options: (i) we set the average phase condition

$$q_H(u) := \sum_{i=1}^{m-1} \langle \partial_x u_*, u(t_i)\rangle = 0, \quad (31)$$

where $u_*{=}u_*(x)$ is a reference profile (usually $u_* = u_H$, the spatial profile at the Hopf point), and $t_1{=}0, t_2\ldots, t_m{=}T$ are the grid points of the time discretization (where internally we rescale $t \mapsto t/T$ to have a fixed time–interval $t \in [0,1)$). In this case, s in (29) is a constant (average) speed, which we can also plot in bifurcation diagrams (BDs). Altogether we have a nonlinear eigenvalue problem for $u = u(x,t)$ and the scalar quantities s and T, consisting of (29), (31), the periodicity condition $u(\cdot,0) = u(\cdot,T)$, and the temporal phase condition (33) below.

Alternatively, (ii) we can use a t–dependent speed $s(t)$, i.e., $\xi = x - \sigma(t)$ and $s(t) = \dot\sigma(t)$, and the pointwise phase conditions

$$q_H(u,t_i) := \langle \partial_x u_*, u(t_i)\rangle = 0 \quad (32)$$

at each t_i, yielding a nonlinear system for $u(x,t)$, $s(t)$ and T. In BDs we can again plot the mean speed $s{=}\frac{1}{T}\int_0^T \dot\sigma(\tau)\,\mathrm{d}\tau$. In most problems considered thus far, both approaches work similarly, and we have mostly used approach (i) [Uec21, Chapter 7]. However, here approach (ii) is more robust and leads to faster convergence of Newton loops and allows larger stepsizes, which is particularly important in the 2D case, where all of the above applies in a rotating frame, i.e., with $s\partial_\vartheta u$ instead of

$s\partial_x u$ on the rhs of (29), with phase conditions of the form $\langle \partial_\vartheta u_{\rm old}, u\rangle = 0$ together with the appropriate modification for PO computation. Finally, since (29) is autonomous, for POs we always need and use the standard temporal phase condition

$$\int_0^T \langle u(\cdot,t), \partial_t u_{\rm old}(\cdot,t)\rangle \,\mathrm{d}t = 0. \tag{33}$$

In all cases we use arclength continuation, where the independent parameter is the arclength ζ along a branch, and u and the primary active parameter (here λ), and possibly further parameters such as s and T, are the dependent unknowns; this allows the computation to pass around folds and in particular to follow "snaking" branches that oscillate back and forth in λ.

Importantly, the gauge invariance of (1) also allows us to compute SWs as relative equilibria, bypassing the PO setup. For this we let

$$u(x,t) = v(x)\mathrm{e}^{-\mathrm{i}\omega t} \tag{34}$$

and obtain the steady state problem

$$\begin{aligned} 0 =&(\lambda+\mathrm{i}\nu)v - (c_3+\mathrm{i}\gamma)|v|^2 v - |v|^4 v \\ &- (1+\partial_x^2)^2 v + \mathrm{i}\delta\partial_x^2 v + s\partial_x v + \mathrm{i}\omega v, \end{aligned} \tag{35}$$

where ω is a now a second nonlinear eigenvalue, in addition to the speed s in (29). The associated phase condition is

$$\langle v, \mathrm{i}v_{\rm old}\rangle = 0 \tag{36}$$

and arises from the derivative $v \mapsto \mathrm{i}v$ of the gauge rotation $v \mapsto \mathrm{e}^{\mathrm{i}\theta}v$ at $\theta = 0$. This condition is equivalent to the temporal phase condition (33) in a genuine PO setup.

We can also use the above approach to track the linear stability properties of the SW solutions $\zeta \mapsto (v,\lambda,\omega)(\zeta)$ and $s = 0$. This allows us to find BPs to LSWs, and HPs to two–frequency SWs, both with $s \equiv 0$, and Hopf bifurcations to two–frequency LSWs that are also found on the LSW branches. In a genuine PO setup, these would correspond to Neimark–Sacker (or torus) bifurcations, which are numerically notoriously difficult. Moreover, on the LSW branches we find drift bifurcations to LDW branches with $s \neq 0$; these *inter alia* yield rungs between even and odd LSW, cf. Fig. 1(d), or more generally localized drifting waves (LDWs). Numerically, the gauge invariance of (1) is thus of great importance, as the computation of SWs and LSWs as genuine POs is more expensive, particularly in 2D, where the ansatz (34) also works, but the computation of bifurcations to two–frequency POs and LDWs from the SWs and LSWs would normally require a much more elaborate setup.

Remark II.3. a) In principle, the gauge invariance can also be used to simplify the computation of MTWs. The MTWs that bifurcate from a TW branch with wave number k take the form

$$u_{\rm MTW}(x,t) = v(x - s_2 t)\mathrm{e}^{\mathrm{i}(kx-\omega t)}, \tag{37}$$

where s_2 is the speed of the envelope v modulating the TW $\mathrm{e}^{\mathrm{i}(kx-\omega t)}$ that travels with speed $s_1 = \omega/k$. Substituting (37) into (1) we obtain

$$\begin{aligned} 0 =&(\lambda+\mathrm{i}\nu)v - (c_3+\mathrm{i}\gamma)|v|^2 v - |v|^4 v \\ &- (1+\partial_x^2)^2 v + \mathrm{i}\delta\partial_x^2 v + s_2\partial_x v \\ &- 2\delta k\partial_x v + \mathrm{i}(\omega - \delta k^2)v - (1-k^2)^2 v. \end{aligned} \tag{38}$$

Solutions of (38) can then be continued in, e.g., λ, with free s_2, ω and the phase conditions (30) and (36), thereby again avoiding the PO setup. However, we refrain here from using this shortcut, for two reasons: (i) in 1D the computation of MTWs as POs is still rather fast, and the combination (37) and (38) generalizes to 2D only in a rather complicated way; (ii) both (34) and (37) depend crucially on the gauge invariance, and in the interest of generality we do not wish to overexploit this special property of the problem. Note that in reaction-diffusion systems with wave bifurcations we were still able to study analogous branches (SWs, LSWs, TWs, MTWs, the latter yielding a state referred to as "jumping oscillons") despite the absence of gauge invariance [KUY21, KMUY26].

b) For the spatial discretization in both 1D and 2D, we use a piecewise quadratic finite element method (P2-FEM), which for our problems gives better accuracy with similar numbers of degrees of freedom (DoF) than "standard" piecewise linear elements (P1-FEM). In 2D, this is combined with a subdivide–and–project (on constant r) strategy for mesh–generation, needed to prevent symmetry loss during continuation, cf. [VKU21]. In 1D we then typically use between 600 and 1200 spatial DoF, and in 2D between 2000 and 8000 DoF. The time discretization for POs uses finite differences with 50 to 100 points per period. For the DNS we use a linearly implicit time stepper based on the data–structures already set up for the continuation. See "CSH" at [pde25, Tab "Apps"] for further details and download of sources. ⌋

For bifurcation diagrams, we use the norms

$$\|u\|_2 := \left(\frac{1}{|\Omega|}\int_\Omega |u(x)|^2 \,\mathrm{d}x\right)^{1/2} \quad \text{for steady states,} \tag{39a}$$

$$\|u\|_2 := \left(\frac{1}{T|\Omega|}\int_0^T\int_\Omega |u(x,t)|^2 \,\mathrm{d}x\,\mathrm{d}t\right)^{1/2} \quad \text{for POs,} \tag{39b}$$

and the temporal frequency ω and/or the speed s (with $s = \langle s(t)\rangle := \frac{1}{T}\int_0^T s(t)\,\mathrm{d}t$ for variable speeds along one period T).

C. The baseline case

Figure 2 shows BDs and sample solutions for TWs (brown), MTWs (magenta), and SWs (blue), over $\Omega_1 =$

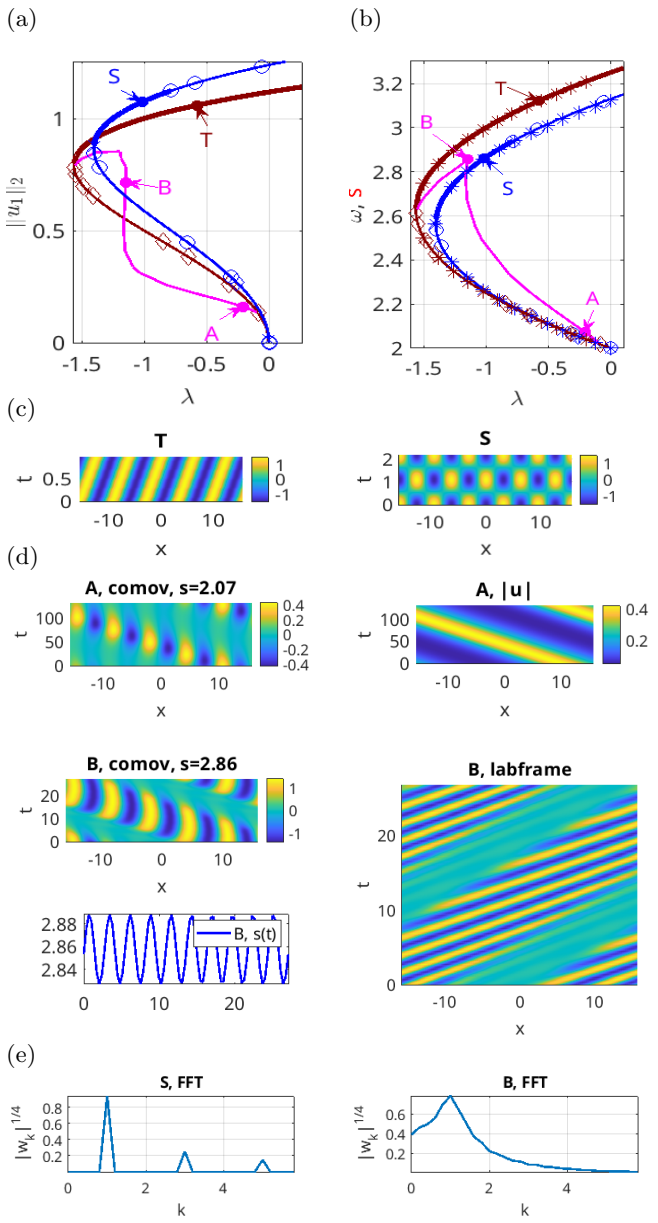

FIG. 2. Solutions of (1) on $\Omega_1 = [-5\pi, 5\pi)$ with $(\nu, \gamma, \delta) = (-1, 0.5, 1)$. (a) BD of TWs (brown, sample state T), SWs (blue, sample state S), and MTWs (magenta, sample states A and B), in terms of the L_2 norms (39). (b) Corresponding speed s (for TWs and MTWs) and frequency ω (for SWs) as a function of λ, together with the exact expression (7) for $s_{\rm TW}$ and the approximate expression (22) for $\omega_{\rm SW}$ ($\star$ symbols). Thick (thin) lines indicate stable (unstable) solutions, except for the MTW branches, where the stability has not been computed. (c) Sample solutions T and S, shown using $\mathrm{Re}(u)$. (d) Sample MTW solutions at locations A and B. For A we show $\mathrm{Re}(u)$ and $|u|$ in the comoving frame with average speed $s \approx 2.07$. For B we also show the instantaneous speed $s(t) = \sigma(t)$, and $\mathrm{Re}(u)$ in the labframe. (e) Power spectra of SW at S and MTW at $t = 0$, location B.

$[-5\pi, 5\pi)$ with λ as the bifurcation parameter and the "base parameter set" (4). Panel (a) shows the normalized L^2 norms (39), while (b) shows the speed s for TWs, and the frequency ω for SWs, together with the exact expression (7) for the TW speed $s_{\rm TW}$ (here $k = 1$, hence $s = \omega/k = \omega$), and the approximate expression (20) for the SW frequency $\omega_{\rm SW}$. Both provide excellent approximations even far from onset. Panel (c) shows $\mathrm{Re}(u)$ for the TW and SW at the locations indicated in (a,b). Note that $|u_{\rm TW}|$ is independent of x, t, as also follows from (7), while $|u_{\rm SW}|$ is only constant in t; the SWs are computed as relative equilibria from the ansatz $u_{\rm SW}(x,t) = v(x)\mathrm{e}^{-\mathrm{i}\omega t}$.

Both TW and SW branches are initially unstable but acquire stability at their respective folds on the left, at the locations predicted in (21) and (23). Both branches exhibit BPs and HPs, indicating the presence of secondary solution branches. Figure 2 shows that the MTW branch (magenta) bifurcates from the first HP on the TW branch at low $\|u\|_2$, and then reconnects to the TW branch near its fold. Panel (d) shows space-time plots of the MTW at locations A and B in (a), where the MTW are computed as relative POs in a comoving frame with variable speed $s(t) = \dot\sigma(t)$ and the pointwise-in-time translational phase condition (32). The first plot shows $\mathrm{Re}(u)$ at A in the comoving frame (with average speed $s \approx 2.07$), while the second plot shows that $|u|$ takes the form of a TW, as already indicated in (37). The resulting solution $u_{\rm MTW}$ is thus a two-frequency state and so is generically nonperiodic in t: in the *comoving* frame it is periodic, however, and exhibits both an oscillation in amplitude and a translation; when this solution is viewed in the labframe, the translation speed changes, resulting in general in a two-frequency state. However, owing to translation invariance of the problem, no frequency locking takes place [Ran82]. For location B we show the solution in both the comoving frame and in the labframe and additionally plot the instantaneous speed $s(t)$; this oscillates about the mean value $s \approx 2.86$. Thus if T is the "round–trip time" of the MTW in the comoving frame, we see that in this frame the envelope travels to the left with speed $-10\pi/T \approx -1.31$ so that its speed in the labframe is approximately $2.86 - 1.31 = 1.55$ which is slower than the mean speed ≈ 2.86 of the underlying wave.

Altogether, the MTW solutions start out as a weak modulation of the TW solution. At location A the envelope is already well-localized but then widens again, with an almost vertical segment (in $\|u\|_2$) around $\lambda = -1.2$, prior to its termination near the TW fold. This abrupt growth in the spatial extent of the structure near $\lambda = -1.2$ indicates an absence of pinning between the fronts on either side of the MTW as the domain fills, and resembles that associated with the presence of a Maxwell point between two homogeneous states in gradient systems. We surmise that this is a consequence of the propagation of the internal structure in the comoving frame which in effect averages out the heterogeneity within the MTW. In contrast, single frequency localized traveling waves (LTWs, also referred to as traveling pulses) may

snake because in the comoving frame the LTW is time-independent [KUY21]. In the present case we have in fact detected slight snaking in the vicinity of $\lambda = -1.2$, behavior we ascribe to weak inhomogeneity arising from asymmetry between the leading and trailing parts of the MTW state.

Finally, panel (e) compares the power spectra (actually $|\hat{u}_k|^{1/4}$) of the SW at location S (for which $|\hat{u}_k|$ is independent of t because $u(x,t) = v(x)e^{-i\omega t}$), and of the time $t = 0$ slice of the MTW at location B (for which $|\hat{u}_k|$ does depend on t but only weakly). The plot for the SW illustrates that all odd modes (here $\hat{u}_k \neq 0$ at $k = 1, 3, 5$) contribute, but the higher modes $k = 3$, $k = 5$ do so much less, a consequence of the strong damping of the linear part of the CSHE35 at larger $|k|$, cf. Remark II.1. On the other hand, for the MTW a continuous band of low wave numbers is involved.

In Figs. 3 and 4 we consider secondary (and tertiary) bifurcations from the SW branch (blue) in Fig. 2(a). These are of three types: a steady-state modulational instability leading to homoclinic snaking, a parity-breaking or drift bifurcation, and a symmetry-preserving Hopf bifurcation. We discuss each of these in turn.

The modulational instability breaks the discrete translation invariance of the SW. The $\Omega_1 = [-5\pi, 5\pi)$ domain admits 5 SW wavelengths, with adjacent cells oscillating out of phase (Fig. 2, state S). Large scale modulation with wavelength 10π can either coincide with the peak oscillation amplitude, leading to a symmetric LSW (LSW^e), or it may coincide with a node at which oscillation is absent, resulting in an odd LSW (LSW^o) consisting of an even number of cells in which adjacent cells oscillate out of phase. These two cases are related by a quarter-wavelength translation of the modulation peak, just as in the real RSHE35 [BK07]. Figure 3 shows both states, labeled A and C, respectively. These states are found on a pair of intertwined branches, even (orange) and odd (green), which bifurcate together from SW at the first BP as the SW amplitude increases, i.e., at finite amplitude. This is a finite size effect, and over $\mathbb{R}$ we expect the LSWs to bifurcate from $u \equiv 0$ at $\lambda = \lambda_c = 0$ simultaneously with the SW branch, much as occurs for steady states in the RSHE35 [BK07]. Both LSW branches start as weak spatial modulations of the underlying SW, but at location A and C the solutions on both branches are already well localized, and subsequently the branches exhibit a number of folds; after each pair of folds another oscillation (i.e., a half-wavelength) is nucleated on either side of the center. Once the domain is filled, the branches reconnect together to the SW branch near its left fold, cf. [BBKM08]. This process resembles closely the *homoclinic snaking* behavior observed in RSHE35 and reflects the presence of pinning of the fronts on either side of the oscillating structure to the heterogeneity in between. Figure 5(b) provides a clearer picture of this behavior on a larger domain. Moreover, the two LSW branches are connected by *rungs*, of which we show one example in red. These rungs arise in drift bifurcations from the odd/even

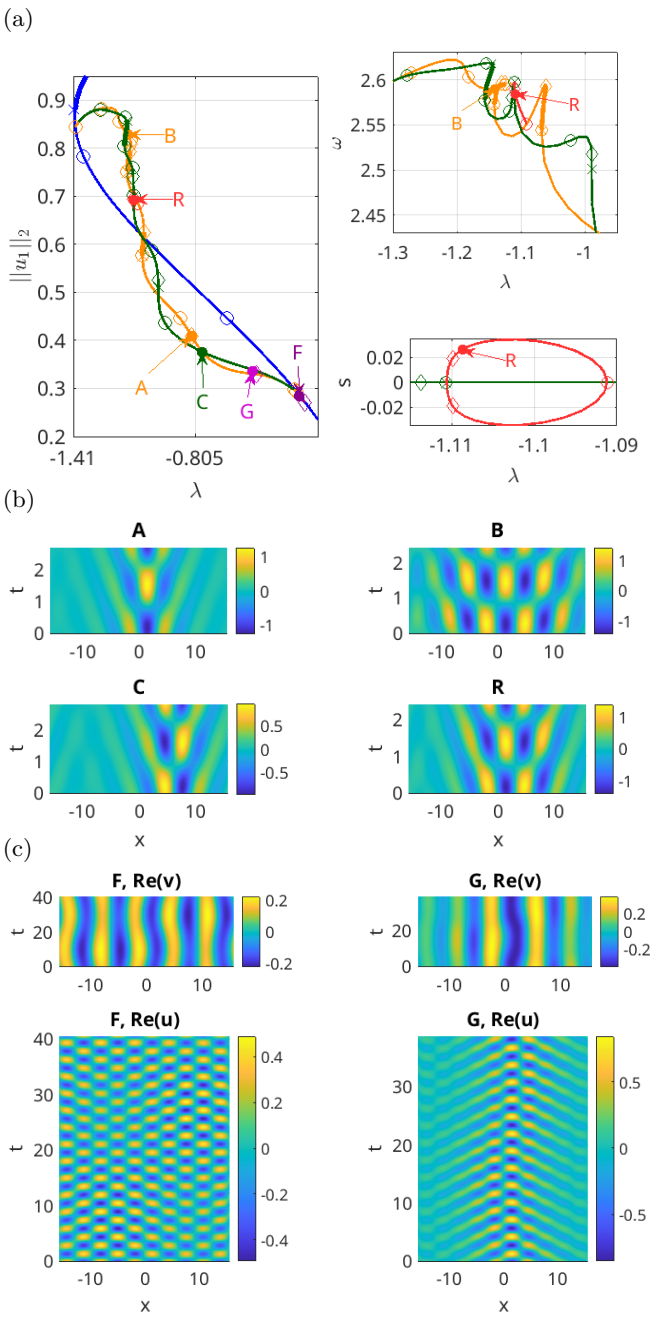

FIG. 3. Solutions of (1) on $\Omega_1 = [-5\pi, 5\pi)$ with $(\nu, \gamma, \delta) = (-1, 0.5, 1)$. (a) Secondary branches of LSW^e (orange, solutions A, B) and LSW^o (green, solution C) and to two-frequency SWs (violet, solution F) together with tertiary branches to rungs (red, solution R) and 2-frequency LSWs (light violet, solution G). (b) Space-time plots showing $\mathrm{Re}(u) = \mathrm{Re}(e^{-i\omega t}v)$ over one temporal period for sample solutions; solution R drifts and so is shown in the comoving frame. (c) Two-frequency SW (solution F) and two-frequency LSW (solution G) in terms of $\mathrm{Re}(v)$ and $\mathrm{Re}(u)$.

LSW, i.e., in steady state bifurcations which break the solution parity and so lead to spatially asymmetric states that drift with a nonzero speed s (see the bottom right panel in (a) for the speed s along a rung branch). The

rungs thus interpolate between odd and even LSW but are neither. Recall that we compute the SWs, LSWs and rung states as steady states v for (35) with ω and s as eigenvalues; in (b) we plot $\mathrm{Re}(u)$ for the reconstructed solution $u(x,t) = v(x)\mathrm{e}^{-\mathrm{i}\omega t}$ for the states labeled in (a). The rung state R is shown in the comoving frame.

Finally, the violet branches in (a) with sample solutions F and G in panel (c) show POs (for v) arising from Hopf bifurcation on the SW and LSW branches, leading to two-frequency states. We continue these branches for relatively short intervals in λ only, as away from onset, the period T of $v(x,t)$ increases rapidly; moreover, all of these two-frequency states appear to be dynamically unstable. For illustration, in Fig. 4 we show DNS from (small perturbations of) the $t = 0$ time slices of F and G. In both cases the solutions converge rather quickly to a TW source–sink mix, a state that also appears to be a generic attractor for (1) with random ICs, at least for the parameter set (4) and $\lambda \in (-0.8, -0.3)$.

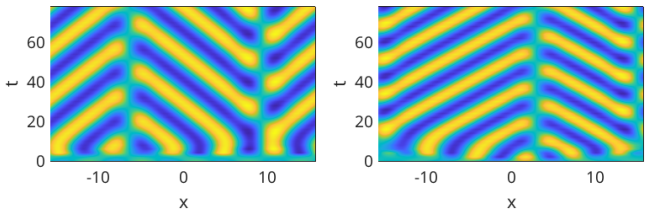

FIG. 4. DNS from the $t = 0$ time slices of the unstable two-frequency states F (left) and G (right) in Fig. 3.

In Fig. 5(a) we run DNS for (1) on the larger domain $\Omega = [-8\pi, 8\pi)$ with an initial condition u_0 consisting of a pair of wave packets. In detail, we let (see the top left panel in (a))

$$u_0(x) = \cos(x)\big[a_1\mathrm{sech}(\frac{x+n\pi}{w}) + a_2\mathrm{sech}(\frac{x-n\pi}{w})\big] \quad (40)$$
$$+\,\mathrm{i}\sin(x+\xi)\big[a_1\mathrm{sech}(\frac{x+n\pi}{w}) - a_2\mathrm{sech}(\frac{x-n\pi}{w})\big],$$

where $n \in \mathbb{N}$ determines the spacing of the two envelope pulses, $a_{1,2}$ specify their amplitudes, $w > 0$ the widths, and ξ is a detuning parameter. Under DNS at $\lambda = -1.1$ (which must be chosen somewhat carefully), these wave packets collide in the middle of the domain and generate a numerically stable LSW^e. The profile at $t = 40$, together with an approximation for ω which can be read off from the period T, can then be used as an initial guess for LSW continuation, resulting in panel (b). The panel shows the resulting LSW^e branch and illustrates its snaking behavior using sample solutions at locations A and B, and identifies many tertiary BPs and HPs, indicating that many further branches are present. Panel (c) shows the results from a similar experiment at $\lambda = -1.2$ starting from an initial condition given by a single wave packet, which under DNS evolves into a MTW. Together, these experiments illustrate the stability (for suitable λ) and the rather large domains of attraction of both LSWs and MTWs.

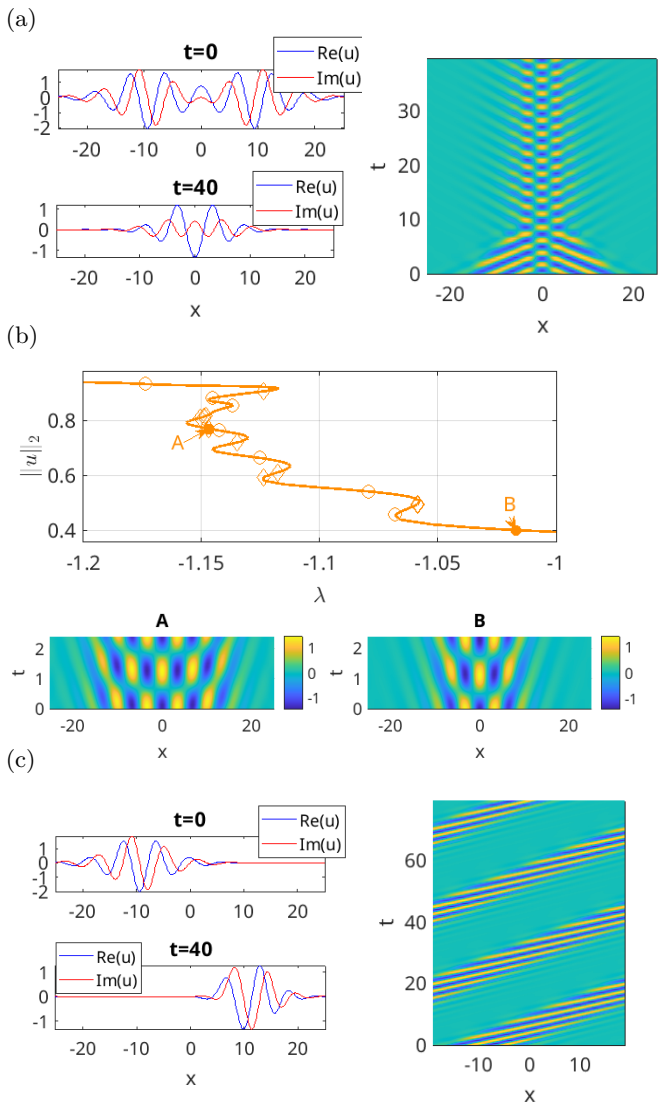

FIG. 5. Solutions of (1) on $\Omega_1 = [-8\pi, 8\pi)$ with $(\nu, \gamma, \delta) = (-1, 0.5, 1)$. (a) Generation of a LSW at $\lambda = -1.1$ from an initial condition with $a_{1,2} = 1$, $n = 3$, $w = 4$ and $\xi = 0$ (upper panel). (b) Continuation of the LSW in (a) to smaller and larger λ, with sample space-time plots at locations A and B. (c) Generation of a right-traveling MTW at $\lambda = -1.2$ from the IC (40) with $a_1 = 1$, $a_2 = 0$, $n = 3$, $w = 4$ and $\xi = 0$ (upper panel). All space-time plots show $\mathrm{Re}\, u(x,t)$.

D. ω decreasing with $|u|$

The solutions in §II C obtained with the "base parameter set" (4), $(\nu, \gamma, \delta) = (-1, 0.5, 1)$ and $c_3 = -2.5$, are characterized by ω_{TW} (via (7)) and ω_{SW} (via the approximation (22), which remains accurate even far from onset), both increasing with the amplitude $|u|$. We now consider the opposite situation where ω instead decreases with $|u|$. For this purpose, we set $\nu = 0$, reduce δ, and employ a negative γ. Figures 6 and 7 explore the case $(\gamma, \delta) = (-0.5, 1)$.

Figures 6(a,b) show BDs of the primary TWs (brown)

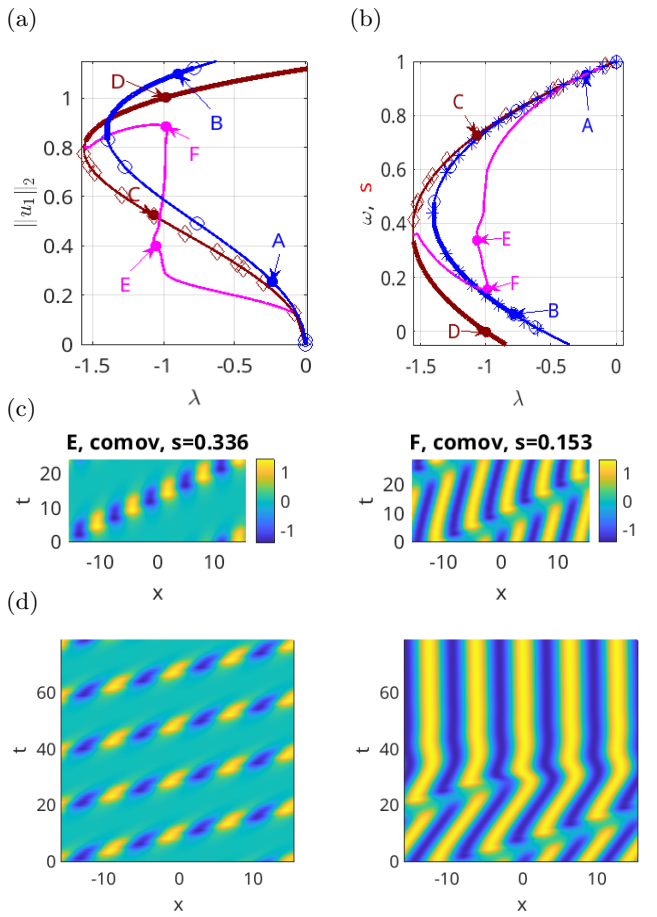

FIG. 6. Solutions of (1) on $\Omega_1 = [-5\pi, 5\pi)$ with $(\nu, \gamma, \delta) = (0, -0.5, 1)$. (a) BD of TWs (brown), SWs (blue), and MTWs (magenta), in terms of the L_2 norms (39). (b) Corresponding frequency ω (for SWs) and speed s (for TWs and MTWs) as a function of λ, together with the approximate expression (22) for SWs ($\star$ symbols). (c) Re(u) for MTWs in comoving frame. (d) DNS from $t = 0$ slices of the states E (stable) and F; the latter converge to TW with almost vanishing speed (state D).

and SWs (blue), and of the first MTW branch (magenta), with sample MTW solutions at locations E and F shown in (c). Although the BD in panel (a) is quite similar to that in Fig. 2(a) the speed $s = \omega$ in panel (b) now decreases along the TW branch, and in particular $s = 0$ near location D at $\lambda \approx -1$. Similarly, ω decreases along the SW branch as predicted by (22), and we find excellent agreement between the approximate expression (22) ($\star$ symbols) and the full numerics, even far from onset, i.e., above the fold in (a). As before, the MTW branch bifurcates from TWs at small $\|u\|_2$ (and large s) and reconnects to the TWs near the fold, with smaller s. However, s is positive everywhere on the MTW branch, and in particular the period T of the MTW solutions in the comoving frame remains bounded, which is why we can continue the MTW branch until its reconnection with the TW branch. In the nearly vertical segment near $\lambda = -1$ the MTW envelope expands rapidly (compare solutions E and F), although this segment in fact contains four folds, and state E is numerically stable (see (d), left panel). On the other hand, F is unstable, and starting near F (with $\lambda_1 \approx -0.98$) yields convergence to the large amplitude TW at this λ and hence a small negative speed $s \approx -0.013$ (state D).

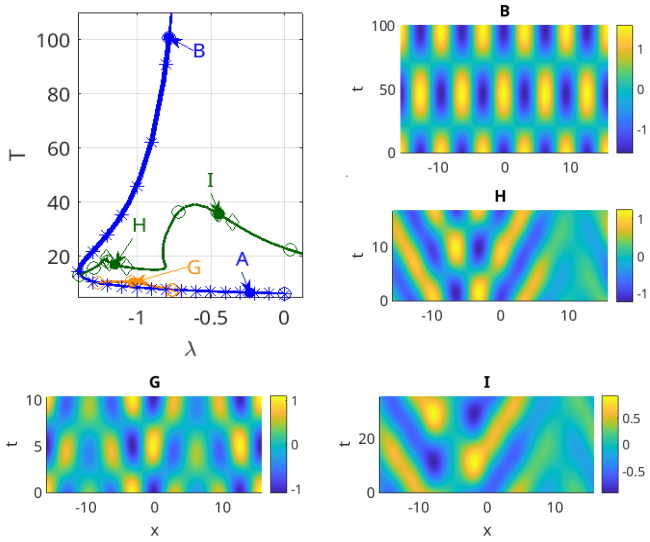

FIG. 7. Solutions of (1) on $\Omega_1 = [-5\pi, 5\pi)$ with $(\nu, \gamma, \delta) = (0, -0.5, 1)$ showing the period T of SWs and LSWs as a function of λ, together with $2\pi/\omega$ from the approximate expression (22) for SWs. A branch of odd LSW states (green, sample solutions H and I) bifurcates from the BP closest to the SW fold and connects to another SW branch with wave number 4/5 that bifurcates from $u \equiv 0$ at $\lambda \approx 0.1296$ (not shown). A branch of two-pulse LSWs (orange, sample solution G) is also shown.

Figure 7 complements Fig. 6 with the corresponding SW and LSW results, showing the period T of the SWs as a function of λ (blue, sample solution B) together with T from the approximate expression (22) ($\star$ symbols). It also shows the period T for odd LSWs that bifurcate (together with even LSWs, not shown) from the last BP on the SW branch before its fold at $\lambda \approx -1.4$ (sample solutions H and I). Naturally, as ω decreases along the SW branch, $T = 2\pi/\omega$ increases, and in fact diverges as $\omega \to 0$, at $\lambda_* \approx -0.76$. Interestingly, generic POs exhibiting such a divergence in period cannot be continued beyond λ_* as $T \to \infty$, but in the present case the reformulation (35) of the problem in terms of the frequency ω allows continuation past $\omega \to 0$ with no problem. In particular, at λ_* with $\omega(\lambda_*) = 0$ we simply find a steady state $u = v$, and for negative ω beyond λ_* the branch continues with gauge rotation in the opposite direction.

Remark II.4. In many problems, the divergence of the period $T \to \infty$ for POs is associated with approach to a heteroclinic orbit [Wig88] or a SNIPER bifurcation [Str18]. The situation here completely different: all POs are always single harmonics in t, i.e., $u(x,t)=v(x)e^{-i\omega t}$, and the divergence of $T=2\pi/\omega$ occurs simply because

$\omega \to 0$. ⌋

In contrast to Fig. 3 the odd LSW branch (green) continues from the vicinity of the SW fold to larger λ, but does not reconnect to the ($k = 1$) primary SW branch at low $\|u\|_2$. Instead it connects to the SW branch with *four* wavelengths in the domain (not shown), i.e., with wave number $k = 4/5$, which bifurcates from $u \equiv 0$ at $\lambda = (1 - 16/25)^2 \approx 0.1296$. The even LSW behaves similarly (not shown). Other BPs also lead to odd and even LSW but these do not connect to other SW branches. We show an example (orange, sample solution G, even under reflection in $x \approx 7$) which connects the third and fourth BP on the SW branch. The corresponding odd LSW branch is omitted.

All these LSW branches in turn support additional BPs, yielding drift bifurcations and rung–like structures, as well as HPs, yielding two-frequency LSWs. However, all these LSW solutions, rung states and two-frequency states appear to be dynamically unstable. Moreover, the rung states behave somewhat differently from those in Fig. 3. They do not yield short (drifting) connections between odd and even LSW branches, but rather connect BPs on the same (odd) branch, or wander away from the LSW branch and become LDW branches with MTW characteristics. We illustrate this behavior in detail in Figs. 8 and 9 for the next parameter set.

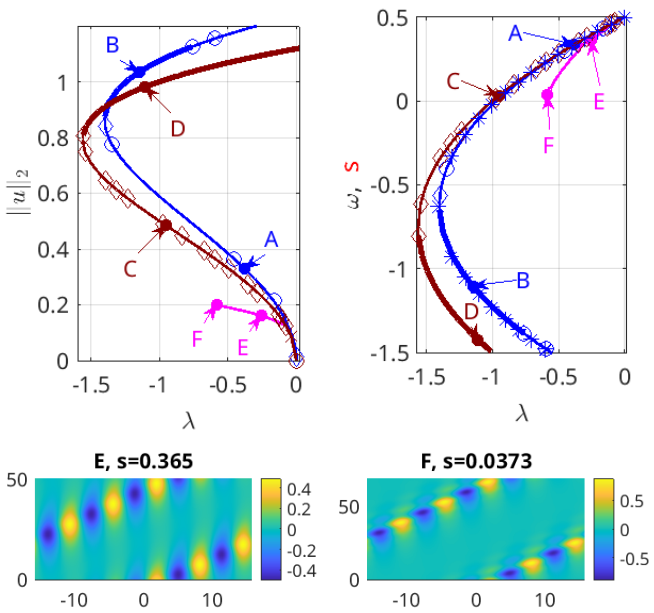

FIG. 8. Solutions of (1) on $\Omega_1 = [-5\pi, 5\pi)$ with $(\nu, \gamma, \delta) = (0, -1, 0.5)$ showing TW (brown) and SW (blue) as a function of λ. The TW speed s now drops to zero before the fold (location C) with similar behavior on the SW branch. The MTW branch (magenta) could not be followed beyond state F because of the long periods T involved.

In Fig. 8 we force a stronger decrease of the speed s with the TW amplitude $|u|$ by taking $(\gamma, \delta) = (-1, 0.5)$. With $\nu = 0$ (7) now shows that $s = 0$ at $\lambda = -13/16 = -0.8125$, i.e., before the TW fold. For these parameters the same happens along the SW branch, i.e., $\omega = 0$ before the SW fold, and this is so in both the numerics and the approximation (22). This fact impacts our numerical continuation of the MTWs (magenta): as s decreases, the period T of the MTWs in the comoving frame increases, and beyond F their continuation became too expensive, and was stopped. In fact the gauge–invariance setup (38) could in principle be leveraged to continue the MTW solutions further, but this has not been implemented here.

Figure 9 shows the BD of some LSW branches, and of tertiary bifurcations from these to localized drifting waves (LDWs). The first BP on the primary SW branch gives rise to the green branch of odd LSWs, together with a similar even LSW branch (not shown). The odd LSW branch becomes stable after a fold near $\lambda \approx -1$, and remains stable until $\lambda \approx -0.6$ (roughly where the large amplitude SWs also lose stability), and then continues to $\lambda > 0$. The second BP on the SW branch generates the light green branch of two-pulse LSWs, i.e., a branch of two equispaced copies of the dark green odd LSW oscillating out of phase. The violet LDW branch, with sample solutions E (and E′), F and G, no longer connects to an even LSW branch, but instead continues to large $|s|$, where the solutions resemble MTWs. Here we also illustrate that the drift direction can be changed by going in the opposite direction at the drift bifurcation (E vs E′), see in particular the labframe plots of E and E′, obtained from DNS starting with the respective profiles, both of which are stable as indicated by the thick lines in (a,b). These LDWs have larger speed $|s|$, amplitude, and spatial extent than the MTWs reached in Fig. 8 and are moreover substantially asymmetric, with a larger amplitude at the leading edge. We currently do not know how the MTW states like those in Fig. 8 and the LDW states like those in Fig. 9 relate to one another, and in particular whether in some parameter regimes they may be connected.

Figure 9 also shows that the LDW branch exhibits behavior akin to collapsed snaking, i.e., it exhibits effects of weak pinning that decreases with increasing width of the state, and that more strongly localized LDWs can be stable (thick lines). State G shows the behavior that arises when the domain is almost filled but the basic wavelength does not quite fit in the domain, leading to frustration. The branch of LDWs bifurcating from even LSW shows similar behavior, but does not contain stable states, and continues to larger λ without frustration, with four wavelengths even at large λ.

Figure 10 illustrates the dynamics for ICs of type (40) on a larger domain, where (a) for $\delta = 0.5$ a head-on collision of two symmetric wave packets generates an even LSW, or equivalently a localized source. On the other hand, (b) for $\delta = 2.0$ ICs in the form of a wave packet generically lead to narrow (strongly localized) MTWs/LDWs, or equivalently to a traveling breather. A similar influence of the parameter δ can also be found for other γ values (and indeed for other parameters): smaller

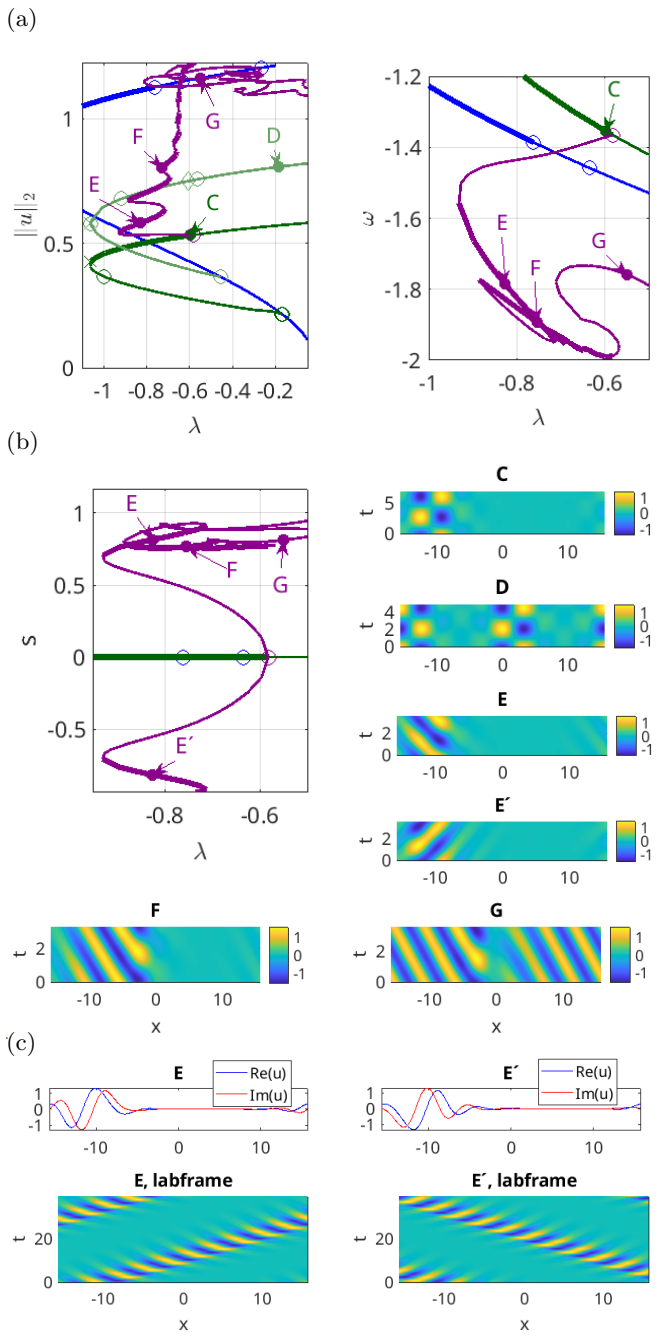

FIG. 9. LSWs and tertiary branches for (1) on $\Omega_1 = [-5\pi, 5\pi)$ with $(\nu, \gamma, \delta) = (0, -1, 0.5)$. (a) BD and the corresponding frequency ω for SWs and LSWs. (b) Sample LSW solutions at locations C (single pulse odd LSW) and D (two-pulse odd LSW) together with the speed s of DSW and sample solutions at locations E, E′ and F. (c) DNS from states E and E′ showing that both are numerically stable.

δ generally favors stable LSWs, while larger δ leads to stable MTWs/LDWs. A more systematic study of this behavior via continuation of LSWs and MTWs/LDWs in δ is possible but is beyond the scope of this work.

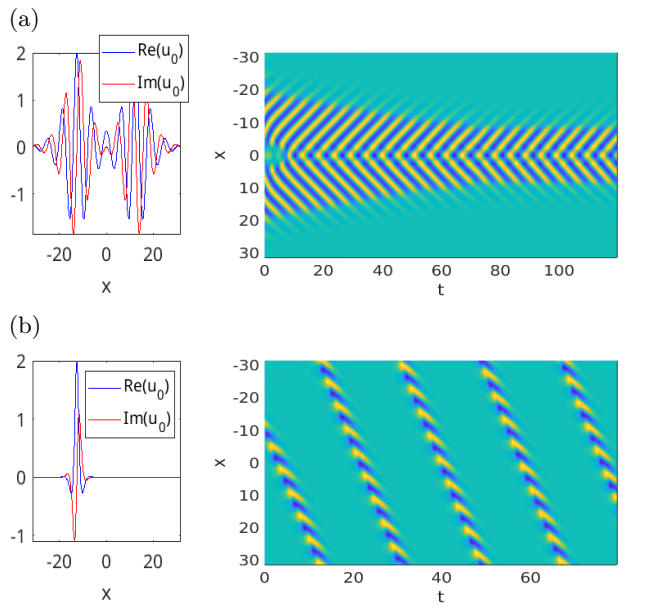

FIG. 10. DNS of (1) on the larger domain $\Omega_1 = [-10\pi, 10\pi)$ with ICs of the form (40) and parameters $(\nu, \gamma) = (0, -1)$, $\lambda = -0.55$. (a) $\delta = 0.5$, $a_1 = a_2 = 2$, $w = 4$, $n = 4$, yielding a stable localized source. (b) $\delta = 2$, $a_1 = 2$, $a_2 = 0$, $w = 1$, $n = 4$, yielding a stable MTW.

III. 2D CASE: FINITE DISK

In the study [VKU21] of the variational cubic-quintic Swift-Hohenberg equation RSHE35 on a disk, we were able to relate many of the 1D steady patterns to the corresponding wall modes on a disk. These "daisy" states were found to localize not only to the wall but along the wall as well, resulting in states of both odd and even parity organized in snaking structures closely resembling those familiar from 1D. Moreover, we were able to study their interaction with bulk states that also form in this system. Motivated by this, we now turn to the CSHE35 on a disk. We aim to understand the bifurcation structure of rotating and oscillating daisies attached to the perimeter of a disk, and the accompanying localized structures along portions of the perimeter. Inevitably, the overall bifurcation picture of solutions on a disk is *much* more complicated, including states that form oscillating and rotating patterns in the bulk of the disk, and their interaction with wall states; however, the bulk states will be discussed only briefly, see Figs.16 and 18.

In 2D traveling waves become rotating waves (RWs), and the MTWs become modulated RWs (MRWs); we keep the name (and acronym) LDW for solutions arising in drift bifurcations from LSWs, where rotation and drift refer to rotations $R_\vartheta u(\cdot) = u(R_\vartheta \cdot)$, with $R_\vartheta = \left(\begin{smallmatrix} \cos\vartheta & -\sin\vartheta \\ \sin\vartheta & \cos\vartheta \end{smallmatrix}\right)$. The speed s is now the rotation speed or angular velocity, and we consider

$$\begin{aligned} \partial_t u =& (\lambda + \mathrm{i}\nu)u - (c_3 + \mathrm{i}\gamma)|u|^2 u - |u|^4 u \\ & - (1+\Delta)^2 u + \mathrm{i}\delta\Delta u + s\partial_\vartheta u, \end{aligned} \tag{41}$$

where $\partial_\vartheta u = (-y\partial_x + x\partial_y)u$. The RWs are computed as equilibria of (41) together with the phase condition $\langle \partial_\vartheta u_{\rm old}, u\rangle = 0$, and for MRWs and LDWs the phase conditions (31) and (32) for the (average) rotation speed translate straightforwardly to the disk case. The gauge invariance $u \mapsto \mathrm{e}^{\mathrm{i}\alpha}u$ is independent of the domain, and so (35), (36) apply to 2D directly.

A. Linear stability, and amplitude equations for RWs and SWs

The eigenfunctions of the Laplacian on a disk of radius R with Neumann BCs at $r = R$ are, in polar coordinates (r, ϑ),

$$u_{m,\ell}(r,\vartheta) = J_m(k_{m,l}r)\exp(im\vartheta),$$

$m \in \mathbb{Z}$, where J_m is the mth Bessel function of the first kind, $k_{m,\ell} = \alpha_{m,l}/R$ and $\alpha_{m,l}$ is the lth zero of J'_m. Thus $\Delta u_{m,\ell} = -k^2_{m,\ell}u$ and hence the linearization of (1) has solutions $u(r,\vartheta,t) = \mathrm{e}^{\mu(m,l)t}u_{m,l}(r,\vartheta)$ with

$$\mu(m,l) = \lambda - (1-k^2_{m,l})^2 + \mathrm{i}(\nu - \delta k^2_{m,l}), \qquad (42)$$

similar to (12). The modes $u_{m,l}$ provide an orthogonal basis of $L^2(\Omega)$ under the scalar product

$$\langle u, v\rangle = \int_0^{2\pi}\int_0^r u(r,\vartheta)\overline{v}(r,\vartheta)r\,\mathrm{d}r\,\mathrm{d}\vartheta. \qquad (43)$$

At this level, the main difference between 1D and 2D is that even for moderate R there are in general many near critical modes $u_{m,l}$ (small $|\mu(m,l)|$), and the order of appearance of the individual modes $u_{m,l}$ with increasing λ depends sensitively on R. See, e.g., [VKU21, §II.A] for details of the spectral analysis (in the real case), and for illustrations of the eigenfunctions at criticality for different R. The bifurcations from $u = 0$ at λ_c are generically double (except in the axisymmetric case $m = 0$), and as a result each bifurcation with $m \neq 0$ leads to both (clockwise or counterclockwise) rotating waves (RWs) and to standing waves (SWs) as equal amplitude superpositions of the RWs, just as in 1D.

Amplitude equations for the RW and SW may be derived analogously to §II A: we pick integers (m, l), $m \neq 0$, and make the single mode ansatz

$$u = (vu_{m,l} + wu_{-m,l})\mathrm{e}^{-\mathrm{i}\omega_{m,l}t}. \qquad (44)$$

Substituting (44) into (1) and projecting back onto $u_{m,l}$ and $u_{-m,l}$ via (43) leads to

$$\begin{aligned} I_1\dot v =& \mu(m,l)I_1 v - (c_3+\mathrm{i}\gamma)I_3(|v|^2+2|w|^2)v \\ &- I_5(|v|^4+3|w|^4+6|v|^2|w|^2)v, \qquad (45a)\\ I_1\dot w =& \mu(m,l)I_1 w - (c_3+\mathrm{i}\gamma)I_3(|w|^2+2|v|^2)w \\ &- I_5(|w|^4+3|v|^4+6|w|^2|v|^2)w, \qquad (45b)\end{aligned}$$

with λ in $\mu(m,l)$ replaced by $\lambda + i\omega_{m,l}$ and $I_j \equiv \int_0^R |J_{m,l}(k_{m,l}r)|^{j+1}r\,\mathrm{d}r$. For simplicity, we evaluate the integrals I_j numerically. For instance for $R = 5$ the primary bifurcation has m=4, $l = 1$, and k_c=1.065, which yields

$$I_1 = 0.211, \quad I_3 = 0.024, \quad I_5 = 0.003. \qquad (46)$$

In any case, we can now analyze (45) exactly like (18). Setting $v = r_1\mathrm{e}^{\mathrm{i}\phi_1}$ and $w = r_2\mathrm{e}^{\mathrm{i}\phi_2}$ we obtain RWs in the form $(r_1, r_2) = (r_{\rm RW}, 0)$ or $(r_1, r_2) = (0, r_{\rm RW})$, with

$$\begin{aligned} r^2_{\rm RW} =& \frac{c_3I_3 \pm \sqrt{c_3^2I_3^2 + 4I_5I_1(\lambda-(1-k^2)^2)}}{-2I_5}, \qquad (47)\\ \omega_{\rm RW} =& -\nu + \delta k^2 + \gamma r^2_{\rm RW}I_3/I_1,\end{aligned}$$

and SWs in the form $r_1 = r_2 =: r_{\rm SW}$ with

$$\begin{aligned} r^2_{\rm SW} =& \frac{3c_3I_3 \pm \sqrt{(3c_3I_3)^2+40I_5(\lambda-(1-k^2)^2)I_1}}{-20I_5}, \qquad (48)\\ \omega_{\rm SW} =& -\nu + \delta k^2 + 3\gamma r^2_{\rm SW}I_3/I_1.\end{aligned}$$

In general, the above expressions for $(r_{\rm RW}, \omega_{\rm RW})$ and $(r_{\rm SW}, \omega_{\rm SW})$ can only be expected to be good approximations close to onset. Nevertheless, we find that even in 2D the single mode ansatz (44) yields very good approximations all the way to $\mathcal{O}(1)$ amplitude, despite the presence of many more only weakly damped modes.

Remark III.1. Going to higher order as in Remark II.1, one finds that $u_{\rm RW}$ with the basic mode m_0, l_0 only contains modes $u_{m_0,l}$, $l \in \mathbb{N}$, and in particular $|u_{\rm RW}|$ is again independent of ϑ and t. Thus, in the following we again mostly plot $\mathrm{Re}(u)$. ⌋

B. The baseline case

Figures 11 and 12 show the resulting wall states on a disk with radius $R = 5$ (perimeter 10π), to be compared with the 1D states from Figs. 2 and 3 on an interval of length 10π. Specifically, Fig. 11 shows the primary RW (brown) and SW (blue) branches when $(\nu, \gamma, \delta) = (-1, 0.5, 1)$; these bifurcate together from $u \equiv 0$ at $\lambda \approx 0.017$. Panel (c) shows that this is a $m = 4$ wall mode and shows the resulting SW (top view at location S together with a space-time plot over one SW period along the perimeter).

The RW states also have $m = 4$ (sample solution T, since we want to keep the letter R for rungs) but rotating rigidly with angular velocity s (panel (b) plots $s_{RW} = 2\pi/4\omega_{\rm RW}$ from (48), showing minor discrepancies above the RW fold only). Comparing to the 1D case, here s (around 0.7, say) is smaller, but this is the angular speed, and for $R = 5$ we obtain $s_w = 5s \approx 3.5$ at the wall, which is comparable to 1D.

The first HP on the RW branch leads to the magenta MRW branch whose behavior parallels that of the MTW

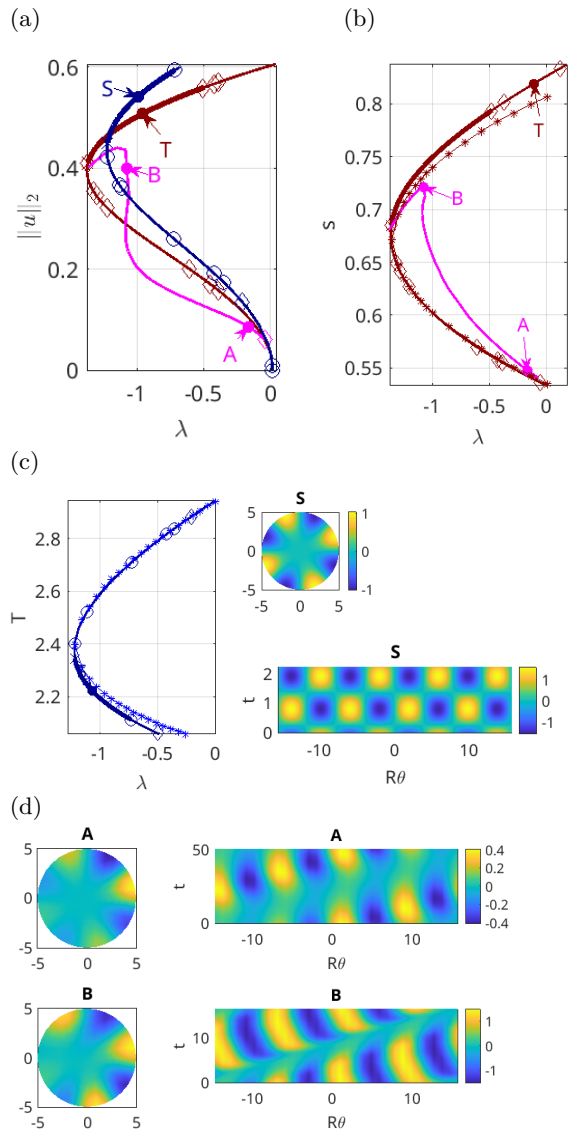

FIG. 11. Solutions of (1) on a disk of radius $R = 5$ when $(\nu, \gamma, \delta) = (-1, 0.5, 1)$ for comparison with Fig. 2. (a) $\|u\|_2$ for RW (brown), SW (blue) and MTW (magenta) as a function of λ. (b) The angular speed s of TW and MTW compared with the approximate expression (47) ($\star$). (c) Period T of SW compared with the approximation (48) ($\star$) together with a sample SW solution at location S (instantaneous profile and dynamics along the perimeter) and a sample RW solution at location T; T has a similar $m = 4$ profile to S and rotates rigidly with angular speed s. (d) Profiles and perimeter dynamics (in the comoving frame) of MTWs at locations A and B. All sample plots show Re(u).

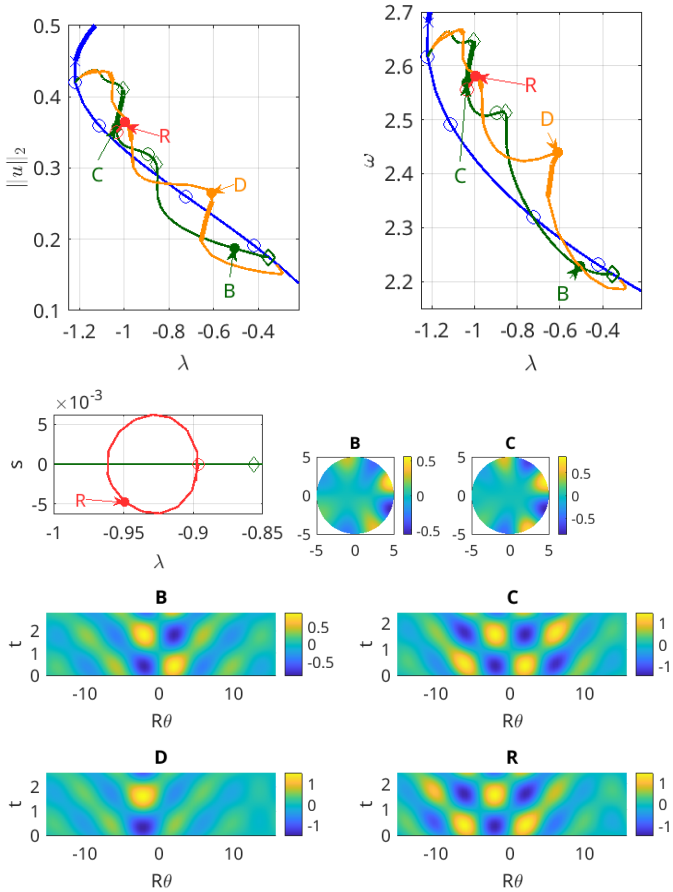

FIG. 12. Even LSW (orange), odd LSW (green) and rung states R (red) together with sample solutions at locations B, C and D in top panels, similar to Fig. 3.

branch in Fig. 2. Moreover, solution B is dynamically stable, and we refer to Fig. 13 for the ξ–t dynamics in the labframe.

Figure 12 shows the secondary bifurcations (open symbols) from the SW branch (with oscillations already localized at the wall) analogous to Fig. 3. In particular, we find branches of even (orange) and odd (green) LSWs, where the "L" stands for localization along the perimeter. In addition, and analogously to Fig. 3, we also find drift bifurcations leading to drifting rung states (red) connecting even and odd LSW branches.

Moreover, there are further HPs on the LSW branches (though here not on the SW branch itself), leading to two–frequency localized states (not shown). Finally, Fig. 13 presents some DNS with ICs in the form of small perturbations of the time $t = 0$ slices of an MRW and an odd LSW, illustrating stability of (these) MRWs and LSWs, and for the MRW illustrating the dynamics in the labframe.

In summary, the primary wall modes and their secondary (and tertiary, e.g., the rungs and two-frequency LSWs) behave fully analogously to the 1D case in Figs. 2 and 3, with one *quantitative* difference: in 1D, the primary bifurcation on an interval of length 10π was to TWs and SWs with wave number $k = 1$ leading to 5 wavelengths in the domain. Here, the primary "daisies" have 4 petals, with the 5-petal daisy bifurcating only at $\lambda \approx 0.421$ (see Fig. 14). This is an effect arising from the dispersion relation (42), i.e., of the extension of the "wall state eigenfunctions" radially into the bulk.

Figure 14 gives a brief overview of some of the subsidiary primary branches bifurcating from the trivial

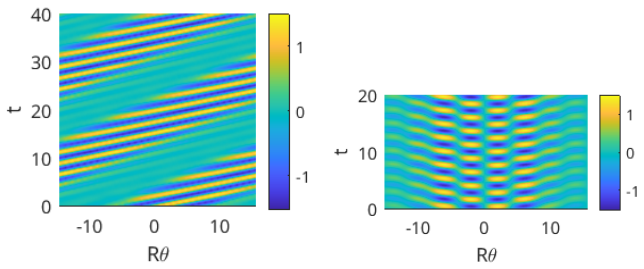

FIG. 13. DNS from the $t = 0$ time slice of solution B in Fig. 11 (left), and from the odd LSW branch (green) in Fig. 12 (right), both at $\lambda = -1.024$.

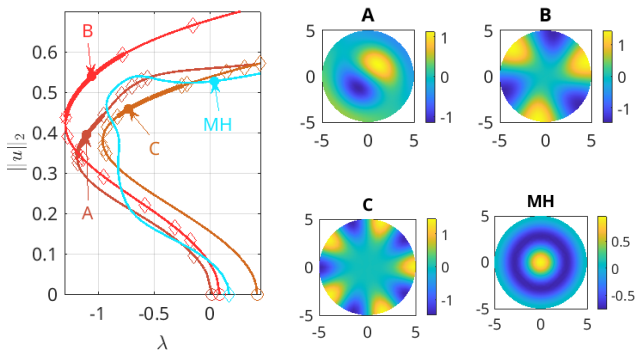

FIG. 14. RW branches bifurcating from the 2nd ($m = 2$, state A), 3rd ($m = 3$, B) and 5th ($m = 5$, C) HP on $u \equiv 0$ together the SW branch bifurcating from the 4th HP ($m = 0$, labeled MH for Mexican hat).

state $u \equiv 0$. In red and brown we display the RW branches bifurcating at the 2nd, 3rd and 5th HP; of these, state A (ying–yang) is a "bulk mode" with $(m, l) = (1, 2)$, while B and C are wall modes with $(m, l) = (3, 1)$ and $(m, l) = (5, 1)$, respectively; each is accompanied by the corresponding SW branch (not shown), with rather more complicated behavior under continuation than the simpler RWs, for example, with "loops" in λ prior to reaching $\lambda > 0$. We show one such SW branch, an axisymmetric "Mexican hat" oscillation with $(m, l) = (0, 1)$. Computations indicate that there are many additional BPs and HPs on both the RW and SW branches but we have not computed the resulting secondary states.

C. ω decreasing with $|u|$

We now switch to the parameters $(\gamma, \delta) = (-0.5, 1)$ and $(\gamma, \delta) = (-1, 0.5)$ for which s and ω decrease with amplitude. Figure 15(a) shows the resulting bifurcation diagram for RWs (brown), SWs (blue, sample solution S), odd LSW (green, sample solution C) and MRWs (magenta, sample solution M). A branch of drifting LSW states (violet, sample solution R) is also shown. Panel (b) shows the associated angular velocity s, while panel (c) shows the SW period $T = 2\pi/\omega$, and compares both with the analytical predictions ($\star$ symbols) from (47) and

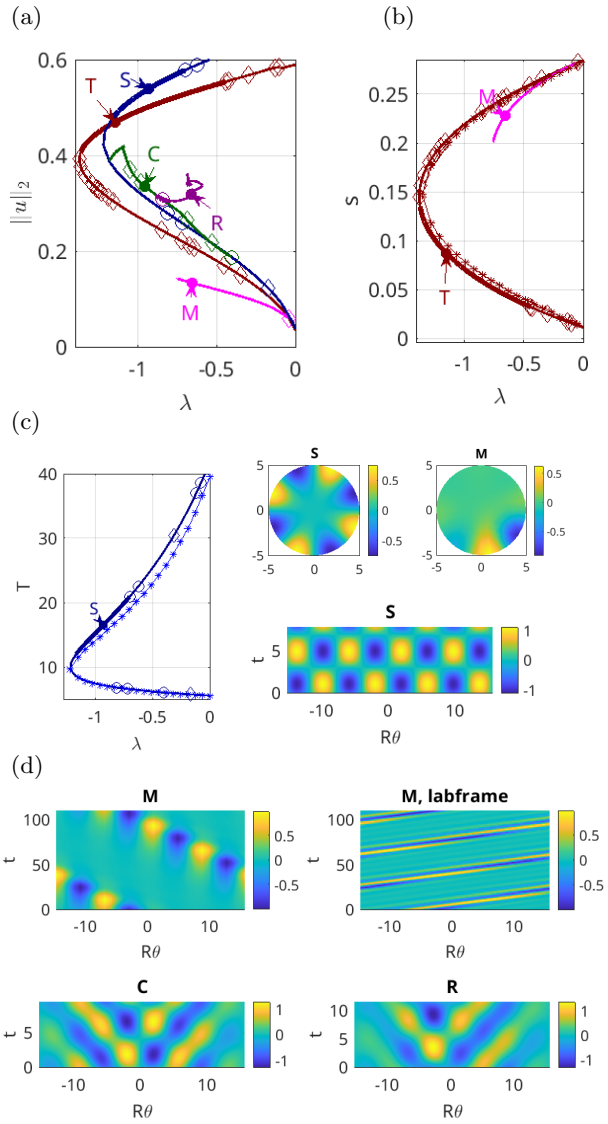

FIG. 15. (a) Solutions of (1) on a disk of radius $R = 5$ when $(\nu, \gamma, \delta) = (0, -0.5, 1)$ for comparison with Fig. 2. (a) $\|u\|_2$ for RW (brown), SW (blue) and MTW (magenta) as a function of λ. (b) The angular speed s of TW and MTW compared with the approximate expression (47) ($\star$). (c) SW period T with approximation (48) ($\star$) and sample SW and MRW solutions at locations S and M, respectively showing profiles (top) and perimeter dynamics for S (bottom); T has a similar profile and rotates rigidly with speed s from (b). (d) Profiles and perimeter dynamics for M, odd localized SW C, and "rung" state R. All plots show Re(u), in the comoving frame for M, R, except the second plot for M.

(48). While the accuracy of these predictions is not quite as good as in the 1D case both the continuation and the predictions show that s decreases along the RW and MTW branches while T increases. In particular, the figure demonstrates that the analytical expressions provide reliable predictions of the solution behavior. Panels (c) and (d) present space-time plots of the solutions at locations labeled in (a).

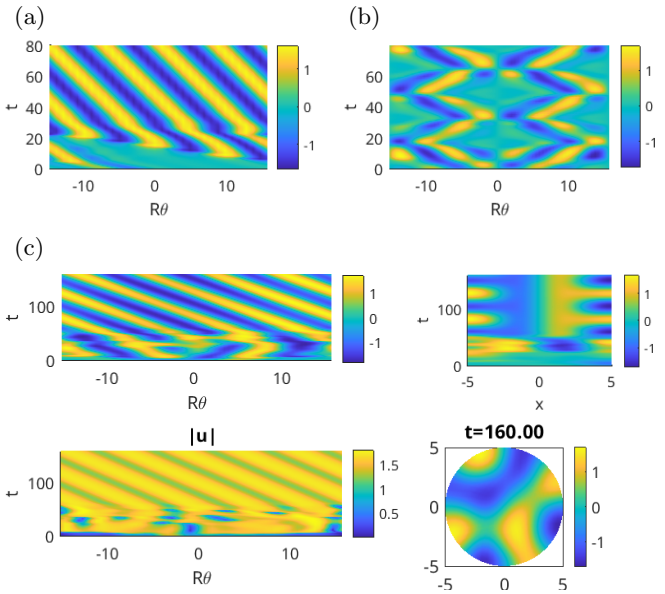

FIG. 16. DNS starting near selected states from Fig. 15. Evolution from (a) M yields convergence to RW; (b) C yields TWs running along the perimeter and colliding repeatedly at ϑ=0 and ϑ=π; (c) R yields waves mostly running along the perimeter but with the bulk also involved, as seen in the plot of $u(x, 0, t)$ ($y = 0$ spatial cut) and $|u|$ along the perimeter, showing significant modulation of profile and speed s, in contrast to the perimeter RWs with constant $|u|$. The last panel shows a snapshot of u at the final time.

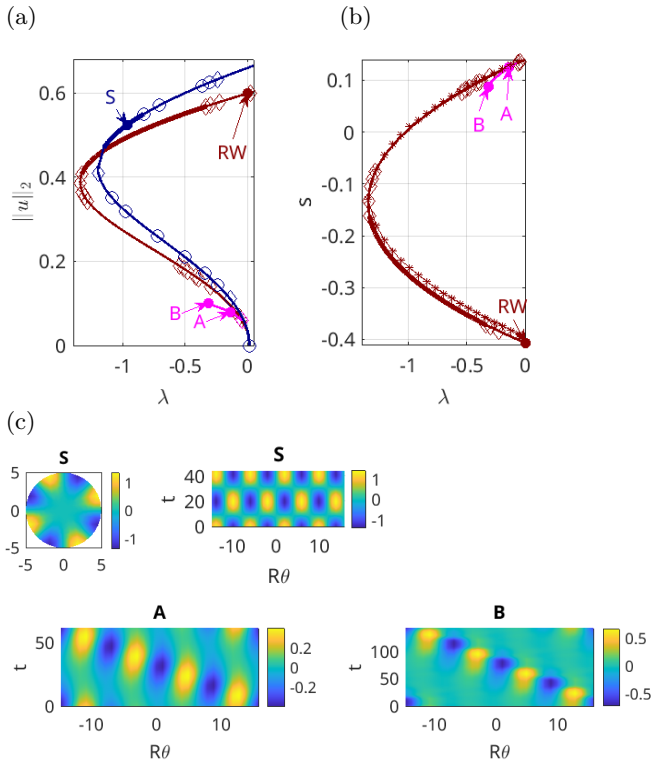

FIG. 17. Solutions of (1) on a disk of radius $R = 5$ when $(\nu, \gamma, \delta) = (0, -1, 0.5)$. (a) $\|u\|_2$ for RW (brown), SW (blue) and MTW (magenta) as a function of λ. (b) The angular speed s of TW and MTW compared with the approximate expression (47) (*). (c) Sample solutions S, RWs A and B in terms of Re(u), in the corotating frame for A, B.

All the secondary and tertiary branches in Fig. 15(a) appear to be unstable, however, and in Fig. 16 we show typical results obtained from DNS initialized from selected unstable states. Panels (a,b) show convergence to wall dynamics, but (c) also illustrates some bulk influence on the dynamics. In this panel the solution attempts to converge to a wall-attached $m = 4$ RW but one of the daisy petals periodically invades the bulk before retreating again, resulting in a two-frequency state with weak modulation of the wall behavior. In particular, for this state $|u|$ is *not* constant (in contrast to a pure RW such as state A) since the periodic expansion of the state is reflected in its angular velocity.

We now discuss the case (γ, δ)=$(-1, 0.5)$ in more detail, starting in Fig. 17 with a brief overview of the results for $R = 5$, followed by larger domain results ($R = 8$) in Figs. 18–20. For $R = 5$, the first RW (brown) and SW (blue) branches behave as before, see Fig. 17(a), but s in (b) (and similarly ω on the SW branch) decays more quickly and reaches zero before either left fold, much as in 1D (Fig. 8). In addition we also computed the first MRW branch (magenta), on which s also decreases rapidly (and the period T in the comoving frame increases). Moreover, as in Figs. 8 and 15, the associated solutions are all unstable: starting with ICs near A or B in panel (a) we obtain convergence to a (stable) RW state, as in Fig. 16(a), but with $m = 5$ (not shown).

For $R = 8$ (with 8400 spatial degrees of freedom), the computation of MRWs as POs in the corotating frame becomes very expensive. Since we expect the MRWs to be in any case unstable, we focus in the following on RWs, and SWs and their secondary bifurcations. In Fig. 18 we show the first RW and SW branches, with $(m, l) = (6, 1)$, bifurcating at $\lambda \approx 0.0146$, together with the second RW branch corresponding to $(m, l) = (3, 2)$ (lighter brown, with sample solutions B, C). This (bulk) branch bifurcates almost simultaneously with the $(m, l) = (6, 1)$ branch, at $\lambda \approx 0.0148$, but does not contain stable solutions up to $\lambda = 0$. Moreover, as we continue to larger amplitudes and/or λ, the rotational asymmetry of u becomes more pronounced, although $|u|$ (not shown) remains constant in ϑ. The second SW branch that bifurcates simultaneously with the second RW is omitted, and also shows no stability gain.

In Fig. 19 we show two secondary bifurcations from the first SW branch to LSWs, and one tertiary bifurcation to a branch of LDWs; the latter play the role of MTWs as in Fig. 9. The green branch corresponds to odd LSWs, with stable solution A, and its subsequent loss of stability yields the violet LDW branch, with the angular velocity s shown in the top right panel. This branch exhibits some snaking behavior, albeit with only one stable segment (solution B), and progressively wider LDW states

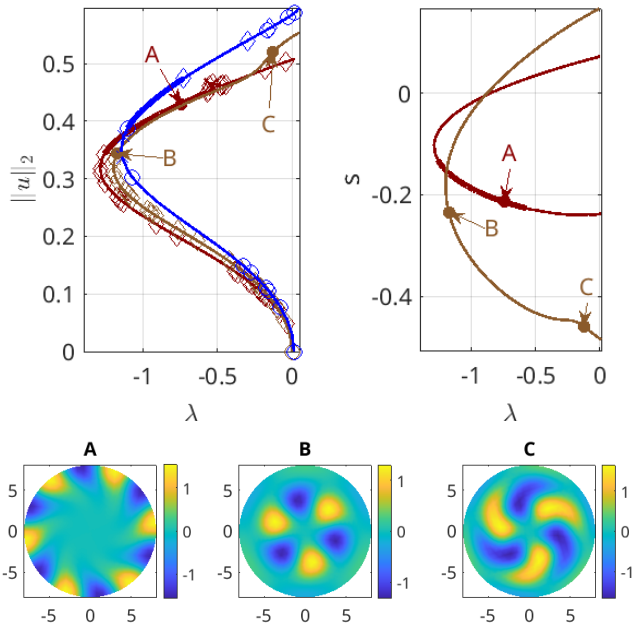

FIG. 18. Solutions of (1) on a disk of radius $R = 8$ when $(\nu, \gamma, \delta) = (0, -1, 0.5)$ showing two primary RW branches (shades of brown) bifurcating at $\lambda = 0.0146$ (wall mode, $m = 6$) and $\lambda = 0.015$ (bulk mode, $m = 3$), together with sample solutions at the locations indicated in the bifurcation diagram. Blue curve shows the SW wall mode.

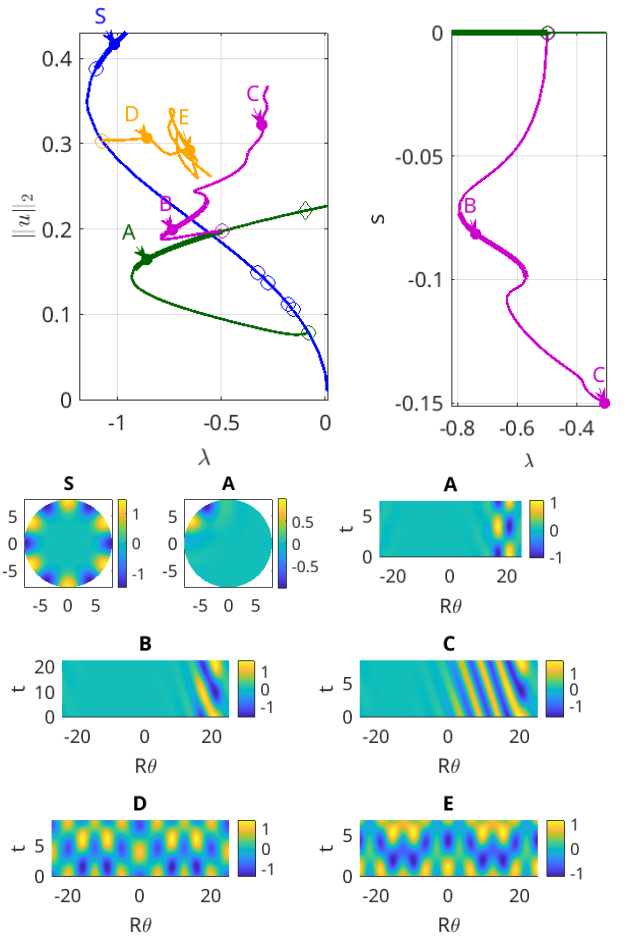

FIG. 19. Solutions of (1) on a disk of radius $R = 8$ when $(\nu, \gamma, \delta) = (0, -1, 0.5)$ showing SWs (blue), odd LSWs (green), tertiary branch (violet) of LDWs, and a branch of more exotic even LSWs (orange). All states are well localized to the wall, as exemplified by states S and A.

as we continue the LDW branch to larger $|s|$ (solution C). DNS starting near C yields convergence to an RW with 8 waves along the perimeter (for $R = 8$ this state bifurcates from $u \equiv 0$ at $\lambda \approx 0.207$), albeit with irregular invasion of the bulk (Fig. 20(a)), yielding a distinct type of modulated RW, while solutions starting near B converge to a "wall only" LDW. Additionally, the orange branch arises from another secondary bifurcation from the SW branch, with a pair of "phase slips" at $\vartheta = 0$ and $\vartheta = \pi$ where $|v|$ becomes small (solution D). At larger λ, $\lambda \in (-0.7, -0.5)$, the branch behaves rather wildly with several loops and profiles resembling solution E. The solutions on the orange branch are all unstable, however, but E can be used as an IC to obtain a combination of two sources and two sinks on the perimeter (Fig. 20(b)), while starting from D yields a stable two-pulse LSW with gaps at $\vartheta = \pm\pi/2$ (Fig. 20(c)).

Finally, in Fig. 21 we use DNS to generate LSWs and LDWs on a larger disk at different λ through initial conditions analogous to (40), namely

$$u_0(r,\vartheta) = c_1 A((R-r)/w_1, (\vartheta-\vartheta_0)/w_2)\mathrm{e}^{\mathrm{i}\vartheta} + c_2 A((R-r)/w_1, (\vartheta+\vartheta_0)/w_2)\mathrm{e}^{-\mathrm{i}\vartheta}, \quad (49)$$

with $A(r,\vartheta) = \mathrm{sech}^2(r)\cosh(R\vartheta)$, $w_1 = w_2 = 4$, $c_1 = 2$, and varying c_2 and ϑ_0 as indicated. The idea is that for $c_2 = 0$ we have a single wave packet, which may or may not converge to a LDW, and which for $c_2 = c_1$ and $\vartheta_0 \neq 0$ will collide with a symmetric wave packet at $\vartheta = 0$, possibly generating a LSW. Figure 21, like the 1D Fig. 5, shows four examples of the various dynamical states that result from this procedure, namely: (a) (rapid) convergence to an LDW at $\lambda = -0.6$; (b) (slower) convergence to an odd LSW from the same ICs as in (a) but for $\lambda = -0.81$; (c) transient generation of an even LSW at $\vartheta = 0$ from two colliding wave packets at $\lambda = -0.8$, but eventual convergence to a source–sink pair; (d) convergence to a stable even LSW at $\lambda = -0.84$ from the same ICs as in (c).

Although additional states can be obtained through further variation of the ICs and the parameter λ (in the range $\lambda \leq -0.6$), these four panels illustrate the four basic solutions types found, all with dynamics confined to the wall. On the other hand, for larger λ, or if $\lambda \in (-1, -0.6)$ for ICs not confined to the wall, one finds a multitude of additional dynamical states involving bulk modes that resist classification.

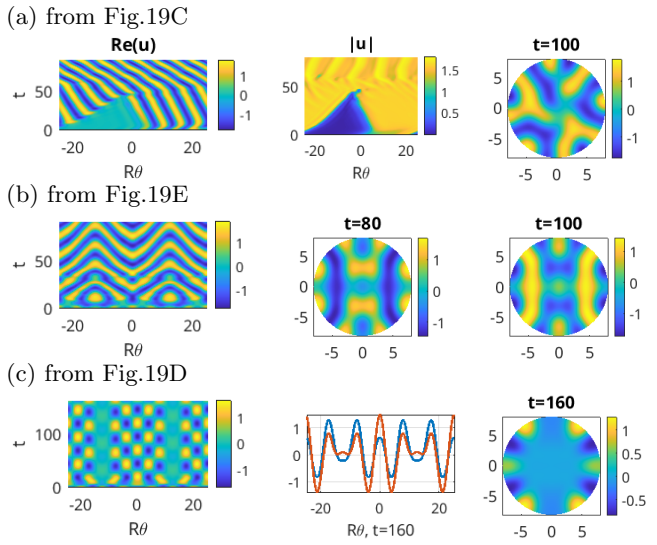

FIG. 20. DNS from near selected states from Fig. 19. (a) Emergence of a modulated RW on the wall, but with significant interaction with the bulk. (b) Emergence of two sources and two sinks on the wall, with waves running through the bulk. (c) Convergence to a two-pulse LSW on the wall, quiet bulk.

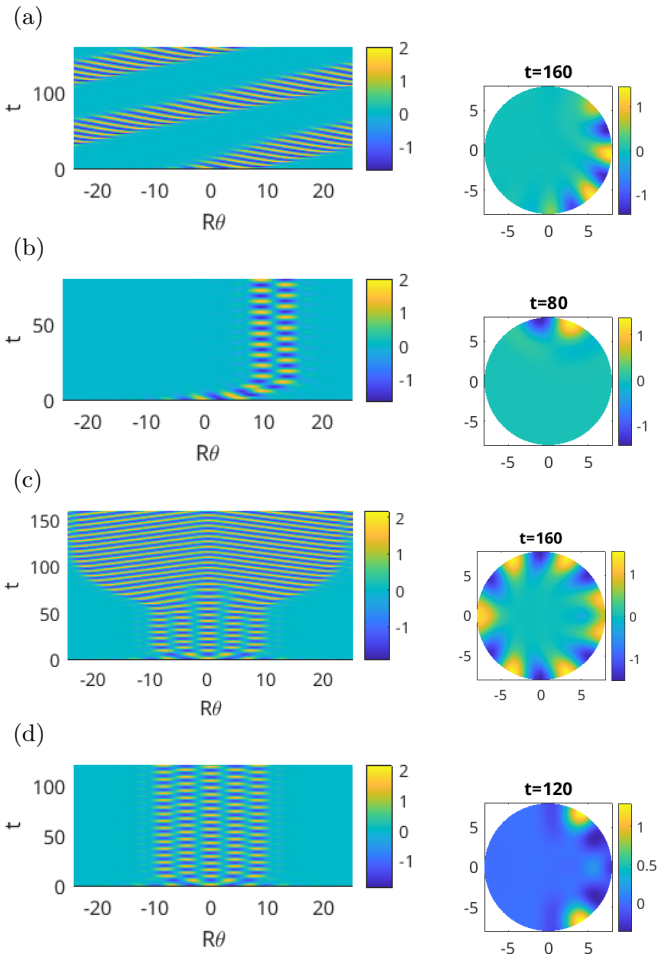

FIG. 21. DNS for $(\gamma, \delta) = (-1, 0.5)$ and ICs of type (49) with: (a) $\lambda = -0.6$, $c_2 = 0$, $\vartheta_2 = 0$, leading to the emergence of LDW like state B from Fig. 19. (b) ICs as in (a), but for $\lambda = -0.81$, leading a narrow transient LDW with eventual convergence to an odd LSW resembling state A in Fig. 19. (c) $\lambda = -0.8$, $c_2 = 2$, $\vartheta_0 = \pi/4$, leading to a collision of two initial MRWs at $\vartheta = 0$ resulting in a transient LSW, which evolves into a source (at $\vartheta = \pm\pi$) sink (at $\vartheta = 0$) pair. (d) Same ICs as in (c) but for $\lambda = -0.84$, leading to convergence to an even LSW. All dynamics are confined to the wall.

IV. DISCUSSION

We have examined in some detail the dynamics of CSHE35 on an interval with pBCs, and on a disk with NBCs. The latter case admits two types of eigenfunctions, wall modes confined to the vicinity of the disk boundary, and bulk modes supported in the bulk, and largely independent of the imposed boundary conditions. We focused here on the subcritical case and showed that the dynamics of the wall states on a disk strongly resemble the behavior identified on a finite interval. Moreover, we showed that this correspondence does not apply only to the primary TW and SW branches, but carries over to secondary localized states, and even to tertiary states. Inevitably, the dynamics on a disk are complicated by the excitation of bulk modes, and we also showed a few examples where bulk modes were intermittently excited. This is particularly so at larger λ ($\lambda > -0.6$, say, i.e., in the less subcritical range). See, e.g., [KMUY26] for an initial discussion of bulk dynamics in a related system, namely an $O(2)$–equivariant RD system on a disk, with wave bifurcation from a spatially homogeneous steady state.

The traveling wave packet states (MTWs and MRWs) are of particular interest. States of this type arise in linear dispersive systems with different phase and group speeds so that crests propagating with the phase speed move through the wave envelope which travels at the group speed, but are also present in nonlinear systems such as binary fluid convection [WIN12]. However, little is known about such nonlinear states and in particular about the bifurcations that lead to them or that allow them to terminate. In the present paper we successfully computed complete branches of MTWs/MRWs (in particular for the base parameter set (4)) and showed that they bifurcate from TW/RW branches at low amplitude and may reconnect with the TW/RW branches at large amplitude (near the respective folds); moreover some of these branches contain stable solutions and exhibit weak snaking characteristics whose origin is not entirely clear. This is in contrast to LSWs, which appear to undergo standard homoclinic snaking whereby each state repeatedly nucleates a new cell on either side of the structure as one proceeds up the branch, much as occurs for steady states in the RSHE35 [BK07]. This behavior can be traced to the reflection symmetry of the SWs from which these states bifurcate and so is ultimately a

consequency of the $O(2)$ symmetry of the probllem. The CSHE35 studied here provides an unambigous example of this type of behavior for time-dependent states, here a spatially localized oscillation, thereby shedding additional light on the snaking of breathers arising in secondary bifurcations of spatially localized steady states [AKNU24, AKMU25].

Another way to obtain traveling wave packets is via drift bifurcation from LSWs. We have identified two distinct types of behavior of the resulting two–frequency states. They may form rung states connecting odd and even LSW branches, characterized by a slow drift speed s, but more generally they take the form of localized drifting waves (LDWs) with an $\mathcal{O}(1)$ speed. The former are present for the parameter set (4) but are typically unstable; the latter are present for parameter sets (10) and (11), and behave much like the MTWs/MRWs. These LDWs may also show homoclinic snaking, with alternating stable and unstable segments of increasing spatial extent, but it is currently unclear whether they terminate in drift bifurcations on other branches of localized oscillations or in Hopf bifurcations on branches of traveling pulses.

The CSHE35 has been studied before, notably in [SB98, GK11], and in the likely related dissipatively perturbed fifth order nonlinear Schroedinger equation ([AA05, SCAA00, DB10] and references therein), but in none of this work have the authors used numerical continuation techniques to identify the origin of the states they found via DNS. In particular, in [SB98] the authors collided oppositely traveling oscillating wave packets and showed that the collision can generate stable localized standing oscillations. A number of states found in [GK11] via DNS resemble those computed here, including bound states of traveling pulses, source-sink pairs and various stationary but pulsating structures. While we are unable to explicitly relate the states identified in [GK11] via DNS to the states computed here via numerical continuation, the work reported in [GK11] exemplifies the dynamical richness of the CSHE35 even when posed on a 1D interval. Of course DNS is only able to identify (numerically) stable structures, and one of the great advantages of the numerical continuation approach adopted here is the ability to compute unstable states as well. These permit one to connect segments of stable states and so establish the origin of many stable structures supported by CSHE35.

Our study was greatly aided by the presence of an $\mathcal{S}^1$ symmetry we referred to as gauge symmetry. This symmetry is present in the CSHE35 (1) but absent in other systems exhbiting a (subcritical) wave instability as the first instability of a spatially uniform state. We were able to exploit this symmetry both in the theory developed here and in the numerics required for numerical continuation of nominally one-frequency and two-frequency states, i.e., TW and SW states as well as drifting oscillating states (MTW/MRW, LDW). In particular the SWs, LSWs and LDWs states could be computed as relative equilibria, an approach that is specific to the CSHE35 and does not generalize to other systems exhibiting a wave instability. However, we expect all these structures to be present in generic $O(2)$-symmetric systems exhibiting a wave instability and have computed such branches in [KUY21, KMUY26]. We also expect tertiary branches (in particular of LDWs) to be present in non–gauge-equivariant systems but these are very expensive to compute without the gauge symmetry.

ACKNOWLEDGMENTS

The work of NV and EK was supported in part by the National Science Foundation under grant DMS-1908891. NV was also funded by the National Agency for Research and Development (ANID) through the Scholarship Program: Becas de Postdoctorado en el extranjero, becas Chile 2018 No. 74190030, and EPSRC via grant EP T017856/1.

[AA05] N. Akhmediev and A. Ankiewicz. Dissipative solitons in the complex Ginzburg-Landau and Swift-Hohenberg equations. In *Dissipative Solitons*, pages 1–17. Berlin: Springer, 2005.

[AK02] I. S. Aranson and L. Kramer. The world of the complex Ginzburg-Landau equation. *Rev. Mod. Phys.*, 74:99–143, 2002.

[AKMU25] F. Al Saadi, E. Knobloch, A. Meiners, and H. Uecker. Breathers and mixed oscillatory states near a Turing–Hopf instability in a two–component reaction–diffusion system. *Physica D*, 472:134482, 2025.

[AKNU24] F. Al Saadi, E. Knobloch, M. Nelson, and H. Uecker. Time-dependent localized patterns in a predator-prey model. *Chaos*, 34:043143, 2024.

[BBKM08] A. Bergeon, J. Burke, E. Knobloch, and I. Mercader. Eckhaus instability and homoclinic snaking. *Phys. Rev. E*, 78:046201, 2008.

[BGP05] P. Blomgren, S. Gasner, and A. Palacios. Hopping behavior in the Kuramoto–Sivashinsky equation. *Chaos*, 15:013706, 2005.

[BK07] J. Burke and E. Knobloch. Snakes and ladders: Localized states in the Swift–Hohenberg equation. *Phys. Lett. A*, 360:681–688, 2007.

[BMvS09] P. Becherer, A. N. Morozov, and W. van Saarloos. Probing a subcritical instability with an amplitude expansion: An exploration of how far one can get. *Physica D*, 238:1827–1840, 2009.

[BT06] K. Borońska and L. S. Tuckerman. Standing and travelling waves in cylindrical Rayleigh-Bénard convection. *J. Fluid Mech.*, 559:279–298, 2006.

[BT10a] K. Borońska and L. S. Tuckerman. Extreme multiplicity in cylindrical Rayleigh-Bénard convection. I. Time dependence and oscillations. *Phys. Rev. E*, 81:036320, 2010.

[BT10b] K. Borońska and L. S. Tuckerman. Extreme multiplicity in cylindrical Rayleigh-Bénard convection. II. Bifurcation diagram and symmetry classification. *Phys. Rev. E*, 81:036321, 2010.

[DB10] O. Descalzi and H. R. Brand. Transition from modulated to exploding dissipative solitons: Hysteresis, dynamics, and analytic aspects. *Phys. Rev. E*, 83:026203, 2010.

[DKJ+00] C. Degen, B. Krauskopf, G. Jennemann, I. Fischer, and W. Elsässer. Polarization selective symmetry breaking in the near-fields of vertical cavity surface emitting lasers. *J. Opt. B: Quantum Semiclass. Opt.*, 2:517–525, 2000.

[DKW81] L. N. Da Costa, E. Knobloch, and N. O. Weiss. Oscillations in double-diffusive convection. *J. Fluid Mech.*, 109:25–43, 1981.

[FK20] B. Favier and E. Knobloch. Robust wall states in rapidly rotating Rayleigh-Bénard convection. *J. Fluid Mech.*, 895:R1, 2020.

[GBM+04] S. Gurevich, H.U. Bödeker, A.S. Moskalenko, A.W. Liehr, and H.-G. Purwins. Drift bifurcation of dissipative solitons due to a change of shape: experiment and theory. *Physica D*, 199:115–128, 2004.

[GHEHR94] M. Gorman, C. F. Hamill, M. El-Hamdi, and K. A. Robbins. Rotating and modulated rotating states of cellular flames. *Combust. Sci. Technol.*, 98:25–35, 1994.

[GK11] L. Gelens and E. Knobloch. Traveling waves and defects in the complex Swift-Hohenberg equation. *Phys. Rev. E*, 84:056203, 2011.

[KM95] K. Krischer and A. Michailov. Bifurcation to traveling spots in reaction-diffusion systems. *Phys. Rev. Lett.*, 73:3165–3168, 1995.

[KMUY26] E. Knobloch, S. Modai, H. Uecker, and A. Yochelis. In preparation, 2026.

[Kno86] E. Knobloch. Oscillatory convection in binary mixtures. *Phys. Rev. A*, 34:1538–1549, 1986.

[KUY21] E. Knobloch, H. Uecker, and A. Yochelis. Origin of jumping oscillons in an excitable reaction-diffusion system. *Phys. Rev. E*, 104:L062201, 2021.

[LMN94] J. Lega, J. V. Moloney, and A. C. Newell. Swift-Hohenberg equation for lasers. *Phys. Rev. Lett.*, 73:2978–2981, 1994.

[LPRT96] M. Le Berre, A. S. Petrescu, E. Ressayre, and A. Tallet. Daisy patterns in the passive ring cavity with diffusion effects. *Opt. Comm.*, 123:810–824, 1996.

[MAB08] I. Mercader, A. Alonso, and O. Batiste. Spatiotemporal dynamics near the onset of convection for binary mixtures in cylindrical containers. *Phys. Rev. E*, 77:036313, 2008.

[Mal84] B. A. Malomed. Nonlinear waves in nonequilibrium systems of the oscillatory type, Part I. *Z. Phys.*, 55:241–248, 1984.

[pde25] pde2path. `https://pde2path.uol.de/`, 2025.

[PGGR97] A. Palacios, G. H. Gunaratne, M. Gorman, and K. A. Robbins. Cellular pattern formation in circular domains. *Chaos*, 7:463–475, 1997.

[Ran82] D. Rand. Dynamics and symmetry. Predictions for modulated waves in rotating fluids. *Arch. Rat. Mech. Anal.*, 79:1–37, 1982.

[SB98] H. Sakaguchi and H. R. Brand. Localized patterns for the quintic complex Swift-Hohenberg equation. *Physica D*, 117:95–105, 1998.

[SCA02] J. M. Soto-Crespo and N. Akhmediev. Composite solitons and two-pulse generation in passively modelocked lasers modeled by the complex quintic Swift-Hohenberg equation. *Phys. Rev. E*, 66:066610, 2002.

[SCAA00] Soto-Crespo, N. Akhmediev, and A. Ankiewicz. Pulsating, creeping, and erupting solitons in dissipative systems. *Phys. Rev. Lett.*, 85:2937–2940, 2000.

[Str18] Steven H. Strogatz. *Nonlinear Dynamics and Chaos: with Applications to Physics, Biology, Chemistry, and Engineering*. CRC press, 2018.

[Uec21] H. Uecker. *Numerical Continuation and Bifurcation in Nonlinear PDEs*. SIAM, Philadelphia, PA, 2021.

[VKU21] N. Verschueren, E. Knobloch, and H. Uecker. Localized and extended patterns in the cubic-quintic Swift-Hohenberg equation on a disk. *Phys. Rev. E*, 104:014208, 2021.

[Wig88] S. Wiggins. *Global Bifurcations and Chaos: Analytical Methods*. Springer Science and Business Media, 1988.

[WIN12] T. Watanabe, M. Iima, and Y. Nishiura. Spontaneous formation of travelling localized structures and their asymptotic behaviour in binary fluid convection. *J. Fluid Mech.*, 712:219–243, 2012.

[ZES93] F. Zhong, R. E. Ecke, and V. Steinberg. Rotating Rayleigh-Bénard convection: asymmetric modes and vortex states. *J. Fluid Mech.*, 249:135–159, 1993.